Materials & Design 258 (2025) 114622

Contents lists available at ScienceDirect

Materials & Design

journal homepage: www.elsevier.com/locate/matdes

Ultra-grain-refinement of face-centered cubic high/medium-entropy alloys: Approaching the limit of grain refinement through severe plastic deformation and recrystallization

Shuhei Yoshida [a,b,*], Nokeun Park [c,**], Kohei Shiotani [d], Yu Bai [a,b,e], Tomoaki Niiyama [d], Akinobu Shibata [a,b,f], Tomotsugu Shimokawa [b,d], Nobuhiro Tsuji [a,b,*]

[a] Department of Materials Science and Engineering, Kyoto University, Kyoto, Japan
[b] Elements Strategy Initiative for Structural Materials (ESISM), Kyoto University, Kyoto, Japan
[c] School of Materials Science and Engineering, Yeungnam University, Gyeongbuk, Republic of Korea
[d] Division of Mechanical Science and Engineering, Graduate School of Natural Science and Technology, Kanazawa University, Kanazawa, Japan
[e] School of Materials Science and Engineering, Dalian University of Technology, Dalian, China
[f] Research Center for Structural Materials, National Institute for Materials Science, Tsukuba, Japan

ARTICLE INFO

Keywords:
Recrystallization
Grain boundary migration
Severe plastic deformation
Deformation structure
High/Medium entropy alloys

ABSTRACT

Face-centered cubic (FCC) high- and medium-entropy alloys (HEAs/MEAs) develop fully recrystallized ultrafine-grained (FRex-UFG) microstructures after simple deformation and annealing processes. However, the mechanistic origins remain unclear. This study explains why FRex-UFG microstructures are readily formed in FCC HEAs/MEAs and clarifies their characteristics of microstructural evolution during deformation and recrystallization. CoCrFeMnNi HEA and CoCrNi MEA were subjected to high-pressure torsion (HPT) followed by short-term annealing. HPT-processed HEA and MEA showed finer nanocrystalline structures with higher dislocation densities than in conventional materials, indicating that dynamic recovery is more inhibited in HEAs/MEAs. Subsequent annealing produced FRex-UFG microstructures with grain sizes (with/without annealing twins) of 410/200 nm and 448/80 nm in the HEA and MEA, respectively, which are the smallest among single-phase materials reported to date. Grain-growth activation energies of the HEA and MEA were three times higher than that of pure Ni. Hybrid Monte-Carlo/molecular-dynamics simulations of grain boundary (GB) structures in model HEAs revealed that severe lattice distortion reduces GB free volume, intensifying solute drag and retarding GB migration. These results demonstrate that inhibited dynamic recovery and sluggish GB migration, both inherent to HEAs/MEAs, elevate the density of potential nuclei for recrystallization while suppressing microstructural coarsening, leading to the formation of FRex-UFG microstructures.

1. Introduction

Heavily deformed crystalline materials store substantial elastic energy owing to the accumulation of nonequilibrium crystal defects, such as dislocations and grain boundaries. Upon high-temperature annealing, microstructural restoration begins with the nucleation and growth of grains with very low defect densities in a process known as *recrystallization*. Recrystallization is one of the most important fundamental phenomena in the fields of physical metallurgy and geology and has been studied for centuries. Recrystallization also plays an essential role in industrial-scale processing of metallic materials because the properties can be finely tuned by controlling the microstructure. In recent decades, the recrystallization mechanism in pure metals and dilute alloys has been extensively studied[1].

High-entropy alloys (HEAs) and medium-entropy alloys (MEAs) are a new class of alloys composed of five or more and four or fewer alloying elements, respectively, in near-equiatomic proportions. These alloys are also called complex concentrated alloys or multi-principal element alloys. In this study, we used the terms HEAs/MEAs, as these are the most widely used and well recognized. These materials have recently attracted the attention of many scientists owing to their intriguing mechanical and functional properties [2–4]. Initially, HEAs/MEAs were

* Corresponding authorsat: Department of Materials Science and Engineering, Kyoto University, Kyoto, Japan.
** Corresponding author at: School of Materials Science and Engineering, Yeungnam University, Gyeongbuk, Republic of Korea.
E-mail addresses: yoshida.shuhei.5s@kyoto-u.ac.jp (S. Yoshida), nokeun_park@yu.ac.kr (N. Park), nobuhiro-tsuji@mtl.kyoto-u.ac.jp (N. Tsuji).

https://doi.org/10.1016/j.matdes.2025.114622
Received 17 June 2025; Received in revised form 29 July 2025; Accepted 20 August 2025
Available online 21 August 2025

predominantly examined in as-cast and as-homogenized states [5]. Subsequently, many groups [6–12] have investigated microstructural changes in HEAs/MEAs during thermomechanical processes involving recrystallization because of their potential industrial applications and fundamental scientific importance. These studies have shown that the microstructures and textures of face-centered cubic (FCC) HEAs/MEAs after cold rolling are similar to those of conventional FCC metals and alloys with low stacking fault energies (SFEs) [10–12]. On the other hand, after annealing, FCC HEAs/MEAs were found to show recrystallization microstructures with a high fraction of annealing twins and relatively random textures [9–13], which is also typical for low-SFE FCC metals and alloys, and to exhibit markedly sluggish grain growth kinetics [10,14–17]. Consequently, fine-grained microstructures can easily be obtained through simple deformation and subsequent annealing processes. For instance, Sun *et al.* [8] reported the fabrication of fully recrystallized (FRex) ultrafine-grained (UFG) microstructures in a CoCrFeMnNi HEA with an FCC single phase via cold rolling and annealing. Our previous studies [6,7,18–20] also demonstrated that FRex-UFG microstructures can be readily achieved in various FCC/BCC MEAs through a severe plastic deformation (SPD) process [21] and subsequent annealing for recrystallization. Grain refinement of these materials has been found to be an effective approach for controlling their properties. The recent emergence of heterostructured materials with multimodal grain-size distributions that exhibit exceptional mechanical properties [22] further illustrates the importance of controlling the microstructure through deformation and recrystallization. Based on these prior works, it would be of interest to reveal the reasons why fine recrystallization microstructures are easily achieved in HEAs/MEAs with FCC structures and to challenge the smallest grain size achievable by recrystallization.

In the present study, we applied high-pressure torsion (HPT) [23], an SPD process, to a CoCrFeMnNi HEA and a CoCrNi MEA (both with FCC structures) at room temperature and investigated their deformation microstructure evolution during the HPT process and recrystallization behavior during subsequent high-temperature annealing. Through a synergistic approach combining experiments and atomistic simulations, we aimed to elucidate the special characteristics of microstructural evolution during deformation and recrystallization in FCC HEAs/MEAs and their mechanisms. In addition, FRex-UFG microstructures with an FCC single phase and the smallest mean grain size ever reported have been achieved. We anticipate that the insights derived in this study will significantly contribute to the development of a comprehensive theory that explains recrystallization and its related phenomena across a wide range of metals and alloys, regardless of the concentration of the alloying elements.

2. Methods

2.1. Materials fabrication

Ingots of an equiatomic CoCrFeMnNi HEA and CoCrNi MEA with a button shape were produced by vacuum arc-melting of the constituent elements with a purity higher than 99.9 wt% in a water-cooled copper mold under an inert argon atmosphere. The buttons were flipped and re-melted at least five times to achieve better compositional homogeneity.

Subsequently, the ingots were cold-rolled to 90 % reduction in thickness and then homogenized (fully recrystallized) at 1200 °C for 24 h under vacuum (approximately 10^{-4} Pa) using a tube furnace to remove elemental segregation in the alloys. Each specimen was subsequently quenched in water, resulting in FCC single-phase microstructures with an average grain size of approximately 50 μm in both the HEA and MEA.

2.2. Deformation and annealing processes

Disk-shaped specimens for high-pressure torsion (HPT) with a diameter of 10 mm and a thickness of 0.8 mm were cut from the homogenized materials. The HPT process was performed at room temperature under a pressure of 6 GPa at a rate of 0.2 rpm (revolutions per minute). The total applied rotation angle was 1800° (five rotations). The shear strain γ applied to the disk specimens during the HPT process can be calculated as

$$\gamma = \frac{2\pi r}{t} N \tag{1}$$

where r is the radial position on the disk, N is the number of rotations, and t is the disk thickness. For instance, the maximum shear strain applied to the materials by five rotations of the HPT was estimated to be as large as $\gamma = 196$.

After heavy deformation by HPT with five rotations, the CoCrFeMnNi HEA and CoCrNi MEA specimens were annealed in a salt-bath furnace under optimized conditions (at 800 °C for 10 s and 700 °C for 30 s, respectively, followed by water quenching) to obtain FRex-UFG microstructures. The grain growth behavior was evaluated by further annealing these FRex-UFG HEA and MEA specimens at temperatures in the ranges of 800 – 950 °C and 700 – 1100 °C (both within FCC single-phase regions), respectively, with varying holding times followed by water quenching. It should be noted that the above temperature ranges were selected because secondary phases such as sigma and hexagonal phases are reported to precipitate at temperatures lower than 800 °C and 600 °C in the CoCrFeMnNi HEA and CoCrNi MEA, respectively [24,25].

2.3. Microstructural observation

Specimens for microstructural observations were cut from the cross-section normal to the radial direction, located 3 mm from the disk center. For scanning electron microscopy (SEM) observations, the specimens were mechanically polished with 1000 – 4000 grit-sized sandpapers followed by diamond paste (1 – 3 μm) to achieve mirror-like surfaces. Subsequently, the specimens were electropolished in a solution comprising 90 vol% ethanol and 10 vol. % perchloric acid at 30 V for 15 s at room temperature. The microstructures of these samples were characterized using SEM (JEOL, JSM-7800F) equipped with a backscattered electron (BSE) detector. The average grain sizes of the specimens were determined from the SEM-BSE images using the line-intercept method. Electron backscatter diffraction (EBSD) measurements were conducted on the CoCrFeMnNi HEA and CoCrNi MEA after primary recrystallization using SEM (JEOL, JSM-7100F) equipped with an EBSD detector. The EBSD data were collected using TSL-OIM data collection software (TSL Solutions, ver. 5.31) and analyzed using OIM analysis software (Tex SEM Laboratories, ver. 7.3).

For transmission electron microscopy (TEM) observations, thin slices were cut and mechanically polished to reduce the thickness to approximately 50 μm. The specimens were electropolished in an electrolyte composed of 70 vol% methanol, 20 vol% glycerin, and 10 vol. % perchloric acid at − 30 °C and at 15 V using a twin-jet polishing machine (Tenupol-5, Struers). TEM observations were performed using JEM-2100F (JEOL) at an operating voltage of 200 kV at room temperature. Selected area diffraction (SAD) patterns of the observed areas were also obtained using an SED aperture with a diameter of 1.5 μm (the largest aperture in the machine) to cover wider regions and many grains.

2.4. X-ray diffraction analysis and dislocation density measurements

To investigate the crystal structure of the HEA and MEA after deformation and after primary recrystallization, X-ray diffraction (XRD) measurements were performed at room temperature (T = 25 °C) in a synchrotron radiation facility, beamline No. 46 XU in the Super Photon Ring – 8 GeV (SPring-8) in Hyogo, Japan. The incident X-ray beam energy was set to 30 keV by employing an automated double-mirror monochromator, and the beam spot size was 0.3 mm (length) × 0.5 mm (width). Disk specimens (with the same shape as the HPT disks) of

the as-HPT and recrystallized materials for the XRD measurements were mechanically polished with 1000–4000 grit fine sandpapers and 1–3 μm diamond pastes to obtain mirror-like surfaces. The final thickness of the specimens for the measurements was approximately 0.5 mm, which is the optimal thickness for obtaining sufficient transmission-diffracted X-ray signals. Each specimen was positioned on a computer-controlled four-axis goniometer to ensure that its position was adjusted precisely to be the same as the designated camera length of the system, and that the disk surface was perpendicular to the incident X-ray beam. The transmission-diffracted X-ray beam was captured using a one-dimensional semiconductor detector (MYTHEN, Dectris). The exposure time was set to 60 s to achieve a suitably high signal-to-noise ratio. The optical system was calibrated by using a standard CeO_2 sample.

The dislocation densities of the deformed materials were estimated using the convolutional multiple whole profile-fitting (CMWP) method [26]. In this process, the XRD profiles were fitted with a theoretical model incorporating the effects of the dislocation density, crystallite size, elastic anisotropy, and planar faults. Because variations in the local chemistry of high-alloy systems, such as HEAs and MEAs, can also contribute to peak broadening (resulting in an overestimation of the dislocation density), the XRD patterns obtained from the fully recrystallized HEA and MEA were used as standards to eliminate the effects of such local chemical heterogeneity, as proposed in a previous study [27].

2.5. Vickers microhardness measurements

Vickers microhardness measurements were performed using a Vickers microhardness tester (SHIMADZU, HMW-2) at a load of 4.903 N with a dwell time of 10 s. All the measurements were performed at room temperature. Disk-shaped specimens of the CoCrFeMnNi HEA and CoCrNi MEA were subjected to high-pressure torsion (HPT) with different numbers of rotations under the same conditions described above. Microhardness measurements were performed on the disk plane of each specimen along the radial direction at intervals of 0.5 mm. The radial position at which each data point was obtained was converted to a shear strain value based on **Equation (1)** to obtain the relationship between microhardness and applied shear strain.

2.6. Atomistic simulations of grain boundaries

To investigate the effect of atomic size differences on the grain boundary (GB) structure in HEAs, we performed hybrid Monte Carlo/molecular dynamics (MC/MD) simulations on two-dimensional crystal lattices composed of five elements with variable atomic sizes. Shifted force potentials ($\phi_s^{\alpha\beta}$) were used to express the interatomic interactions between the two elements α and β in which the gradient becomes zero at the cutoff distance of r_c, as follows:

$$\phi_s^{\alpha\beta}(r) = \begin{cases} \phi^{\alpha\beta}(r) - \phi^{\alpha\beta}(r_c) - (r - r_c)\dfrac{d\phi^{\alpha\beta}(r_c)}{dr} & (r \leqslant r_c) \\ 0 & (r \geqslant r_c) \end{cases} \quad (2)$$

where r is the distance between the atoms of the two elements and $\phi^{\alpha\beta}$ is the Morse potential, expressed as

$$\phi^{\alpha\beta}(r) = D^{\alpha\beta}\left\{e^{-2a^{\alpha\beta}\left(r-r_0^{\alpha\beta}\right)} - 2e^{-a^{\alpha\beta}\left(r-r_0^{\alpha\beta}\right)}\right\} \quad (3)$$

where $D^{\alpha\beta}$, $a^{\alpha\beta}$, and $r_0^{\alpha\beta}$ are the material constants related to the cohesive energy, elastic constant, and lattice constant, respectively. For the sake of simplicity, the values of $D^{\alpha\beta}$ and $a^{\alpha\beta}$ were fixed at 8.16×10^{-20} J and 14.57 nm^{-1}, respectively, for all the elemental combinations. To simulate quinary HEAs with different atomic size differences, $r_0^{\alpha\beta}$ was defined as

$$r_0^{\alpha\beta} = r_0^{33} + \frac{1}{2}k\xi(\alpha + \beta - 6)(\alpha, \beta = 1, 2, \cdots, 5) \quad (4)$$

where r_0^{33} and ξ are 0.4657 nm and 0.067 nm, respectively. Four types of HEAs with different atomic-size differences were simulated by setting k equal to 0, 1, 2, or 3. The value of r_c in **Equation (2)** was set as 2.2 r_0^{55}.

The atomic-size differences in the model quinary HEAs were quantified using the following equation:

$$\delta = \sqrt{\sum_{\alpha=1}^{5} c_\alpha \left(1 - \frac{r^{\alpha\alpha}}{\sum_{\beta=1}^{5} c_\beta r^{\beta\beta}}\right)^2} \times 100 \quad (5)$$

where c_α is the concentration of each element in the simulated model HEAs. $r^{\alpha\alpha}$ is the radius of element α in a perfect crystal relaxed by the method described later and is close to $r_0^{\alpha\alpha} = r_0^{33} + k\xi(\alpha - 3)$. The δ values of the four types of simulated model HEAs (four kinds) were 0, 2.06, 4.12, and 6.15.

We created bicrystal models in which one circular grain was embedded in a matrix to simulate the GB structures in the model HEAs with different δ. The embedded grains were rotated by 30° with respect to the matrix. Five elements (approximately 500 atoms per element) were arranged randomly in a triangular lattice. Periodic boundary conditions and constant stress conditions were imposed on all structures. The thermodynamic equilibrium states of the atomic configurations at finite temperatures (T) were calculated using a hybrid MC/MD method. In this approach, all the atoms were relaxed using MD for 100 ps to create an initial configuration containing relaxed GB structures. Subsequently, the positions of two randomly selected atoms were swapped, and the GB structures were further relaxed for an additional 10 ps using MD. The total potential energy change (ΔE) of the system resulting from this exchange was subsequently calculated, and if $\Delta E \leq 0$, the exchange of atoms was accepted. When $\Delta E > 0$, the exchange is accepted based on the probability of $\exp(-\Delta E/k_B T)$, where k_B is the Boltzmann constant. In each model, the exchange of atoms was carried out 7320 times at $T =$ 300 (equal to approximately 0.1 T_m), 1000 (~ 0.4 T_m), and 2000 (~ 0.8 T_m) K, where T_m (~ 2500 K) represents the average melting point for all models with different δ values. Here, relaxation by the MD method was performed near the athermal limit (1 K) to avoid disturbing the lattice and GB structures by thermal fluctuation.

In each HEA model, the average free volumes at the GBs with different GB misorientations (0°– 60°) were quantified using the following equation:

$$V_{GB} = \frac{1}{A_{GB}}(V_{Cell} - N_{Cell}\overline{V_{Atom}}) \quad (6)$$

where A_{GB} is the total GB area. V_{Cell} and $\overline{V_{Atom}}$ are the total volumes of the simulated unit cell including the GBs and the average atomic volume for a perfect lattice, respectively, and N_{Cell} is the total number of atoms in the simulated unit cell including the GBs. It should be noted that V_{GB} has length dimensions. To adequately compare the results obtained under different conditions, the V_{GB} values were first normalized by the magnitude of the Burgers vector (b) to eliminate the effect of the system size (i.e., V_{GB}/b). Then, the values were normalized again by the value for the pure metal with $\delta = 0$ (i.e., $V_{GB}^{\delta=0}/b^{\delta=0}$), as shown in Fig. 10 **(c)**.

3. Results

3.1. Deformation microstructures after severe plastic deformation

First, we investigated the deformation microstructures of the HPT-processed CoCrFeMnNi HEA and CoCrNi MEA, which were closely correlated with the recrystallization microstructures, as discussed later. In Fig. 1, the microhardness values of the HEA and MEA processed by HPT with different rotation numbers are plotted as a function of the applied shear strain. The microhardness values before HPT are indicated

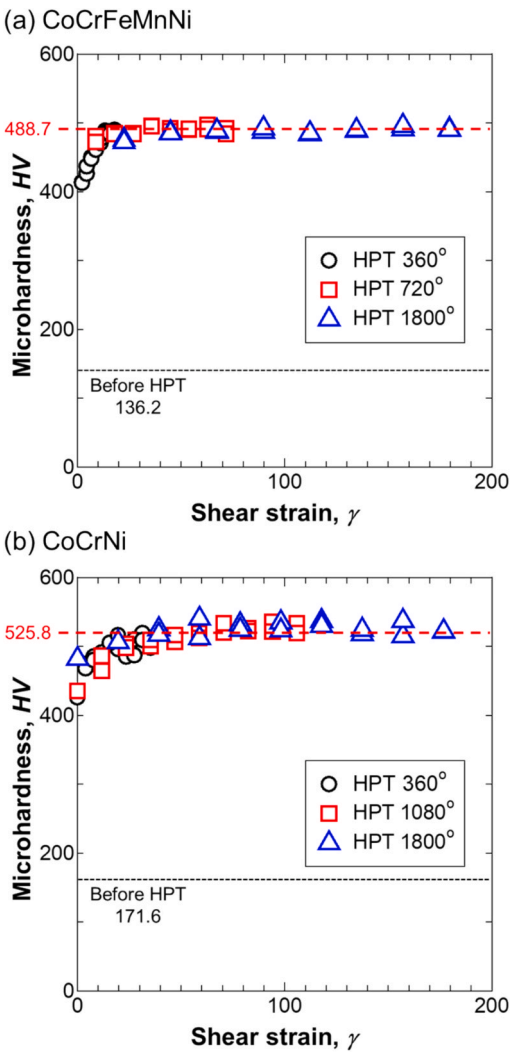

Fig. 1. Microhardness as a function of applied shear strain during HPT under various conditions for the (a) CoCrFeMnNi HEA and (b) CoCrNi MEA. The microhardness prior to HPT processing is indicated in each case by black dashed lines. The microhardness after saturation is also indicated by red dashed line in each figure.

by dashed lines in the plots. In the CoCrFeMnNi HEA, the microhardness increased from HV 136.2 to HV 488.7 and then saturated after a shear strain of approximately 15. In the CoCrNi MEA, the microhardness increased from HV 171.6 to HV 525.8 and then saturated at a shear strain of approximately 20. The saturation of microhardness suggests that the microstructural changes reached a dynamic equilibrium state based on the balance between the introduction of defects and dynamic recovery during HPT [28].

Fig. 2 **(a) and 3 (a)** present bright-field (BF) TEM micrographs showing the deformation microstructures of the HEA and MEA, respectively, after HPT with five rotations. Based on the BF images and corresponding dark-field (DF) images (Fig. 2 **(c, d) and 3 (c, d)**) taken from specific diffraction spots in the SAD patterns (Fig. 2 **(b) and 3 (b)**), nanocrystalline microstructures composed of fragmented grains elongated along the shear direction, with mean thicknesses of 58 and 43 nm, were observed in the CoCrFeMnNi HEA and CoCrNi MEA, respectively. Notably, these grain sizes are much smaller than those typically found in pure FCC metals or dilute alloys processed under similar conditions [29]. Based on the ring patterns in the corresponding SAD patterns (Fig. 2 **(b) and 3 (b)**), it is suggested that there is a large misorientation in the microstructure and that many of the grains are surrounded by high-angle (HA) grain boundaries (GBs). Furthermore, the HEA retained its FCC single phase after HPT, whereas the MEA comprised FCC and HCP phases (diffuse intensity in the SAD pattern shown in Fig. 3 **(e)**). The high-resolution TEM lattice images of the CoCrNi MEA (Fig. 3 **(g) and (f)**) further confirmed the presence of the HCP phase with a plate-shaped morphology. Similar structures have been reported in the same alloy deformed by tensile testing at room temperature and cryogenic temperatures [30,31] and have been attributed to deformation-induced martensitic phase transformation. We also performed synchrotron XRD measurements of the HPT-processed materials to confirm their crystal structures, as shown in Fig. 4. After HPT, the HEA (Fig. 4 **(a)**) exhibited only peaks corresponding to an FCC structure, whereas in the MEA (Fig. 4 **(b)**), the (1 0 0) peak of the HCP structure was observed along with the peaks of the FCC structure. These results were consistent with the TEM results described above.

We employed the CMWP method [26] to extract the dislocation densities of the FCC phase in HPT-processed materials from the XRD profiles shown in Fig. 4. The dislocation densities for the HPT-processed HEA and MEA were estimated to be 3.4×10^{16} m^{-2} and 5.4×10^{16} m^{-2}, respectively, in agreement with previous literature [32]. These high dislocation densities can be attributed to the low SFEs of the HEA and MEA (approximately 30 mJm^{-2} [33] and 20 mJm^{-2} [34], respectively). It should be noted that amorphization can occur at dislocation densities in the range of $10^{17} - 10^{18}$ m^{-2}, as has been reported for the Ni-Ti system [35]. Therefore, the dislocation densities in the HEA and MEA were considered close to their upper limits for maintaining the crystalline structure. As a result, extensive grain subdivision (fragmentation by accumulation of defects) [36] occurs in the materials, leading to very fine nanocrystalline microstructures.

3.2. *Microstructures after primary recrystallization*

We subsequently annealed the CoCrFeMnNi HEA and CoCrNi MEA at 800 °C for 10 s and 700 °C for 30 s, respectively, to obtain FRex-UFG microstructures. Fig. 5 shows the SEM-BSE micrograph of the CoCrNi MEA processed by HPT and subsequently annealed at 700 °C for 10 s, where the material exhibited a partially recrystallized microstructure. Nucleation of recrystallized grains with a grain size of approximately 100–200 nm (excluding annealing twins) was confirmed during this process. We note that partially recrystallized microstructures could not be observed in the CoCrFeMnNi HEA because it was necessary to anneal the specimens at temperatures above 800 °C, where the recrystallization kinetics were very fast, to avoid sigma phase precipitation [24,25].

After annealing the HEA and MEA at 800 °C for 10 s and 700 °C for 30 s, respectively, we obtained specimens with FCC single-phase fully recrystallized microstructures with numerous annealing twins, which can be attributed to the low SFEs, as shown in Fig. 6 **(a) and (c)**. Fig. 6 **(b) and (d)** present the corresponding GB maps without twin boundaries (TBs) drawn based on Fig. 6 **(a) and (c)**. The mean grain sizes (without/with TBs) for the HEA and MEA were measured to be 410/200 nm and 448/80 nm, respectively, using the intercept method on the SEM-BSE images (see **Fig. S1** in the supplementary information for the grain size distribution). Notably, such remarkable ultrafine single-phase microstructures after recrystallization have seldom been reported. To the best of our knowledge, the mean grain size (with TBs) of 80 nm in the MEA is the smallest among the materials with single-phase FRex-UFG microstructures reported to date, such as austenitic steels (> 400 nm) [37], nickel-based alloys (> 320 nm) [6], and copper alloys (> 470 nm) [38]. It should be noted that similar grain sizes (with TBs) were also reported in other FCC HEAs/MEAs [7], such as equiatomic CoCrFeNi MEA (160 nm) and non-equiatomic CoCrNi MEA (110–260 nm) processed by HPT and annealing. Thus, we can conclude that the formation of such an ultrafine microstructure is a general characteristic of HEAs/MEAs. The mechanical properties of the FRex-UFG materials were found to be improved compared to those of the as-HPT materials (see **Fig. S2** and **Table S1** in the supplementary information).

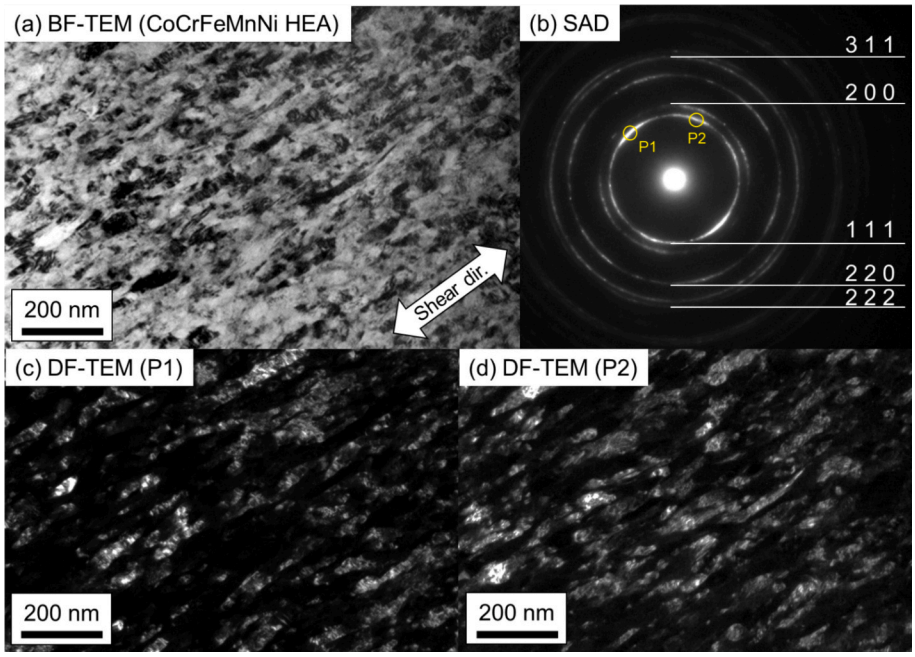

Fig. 2. (a) BF-TEM micrograph of the CoCrFeMnNi HEA processed by HPT. The shear direction is indicated by the double-headed arrow in the figure. (b) SAD pattern acquired from the area shown in (a). The indices of each ring corresponding to an FCC structure are indicated in the figures. DF-TEM images formed by diffraction at the points labeled (c) P1 and (d) P2 in (b) and obtained from the same area as shown in (a). Fragmented grains containing numerous lattice defects and elongated along the shear direction can be seen.

We consider these microstructures of the HEA and MEA to be fully recrystallized immediately after primary recrystallization is completed based on the following evidence:

(1) Equiaxed grain shape.

As shown in Fig. 6 **(a) and (c)**, all grains exhibited an equiaxed shape, in contrast to the elongated shape in the HPT-processed specimens shown in Figs. 2 and 3, and the grain sizes were larger than those of the HPT-processed specimens. This indicates that grain boundary migration and coarsening (recrystallization) occurred in these grains.

(2) Low defect density.

Fig. 7 **(a) and 8 (a)** show the BF-TEM micrographs of the HEA and MEA, respectively, after the annealing process. The corresponding SAD patterns (Fig. 7 **(b) and 8 (b)**) exhibit spot patterns along the radial positions of the FCC structures. This is consistent with the fact that the width of the FCC peaks in the XRD profiles (Fig. 4) drastically reduced compared with the profiles of the HPT-processed specimens, indicating that the density of lattice defects significantly decreased owing to recrystallization. The DF-TEM images (Fig. 7 **(c) and (d)** for the CoCrFeMnNi HEA and Fig. 8 **(c) and (d)** for the CoCrNi MEA) also show that the grains contained a very small number of dislocations and stacking faults, which were thought to remain during the formation process of the nuclei of recrystallized grains.

(3) Grain boundary characteristics.

Fig. 9 **(a, b) and (e, f)** display the EBSD inverse pole figure (IPF) maps and corresponding GB maps for the CoCrFeMnNi HEA and CoCrNi MEA, respectively, after primary recrystallization. The grains in both materials were found to be mostly surrounded by HAGBs, and all grains contained annealing twins. The high fraction of HAGBs is further evidence that growth of the nuclei of recrystallized grains with different orientations occurred and they collided with each other. The length fractions of the TBs were estimated to be 28 % and 35 % in the HEA and MEA, respectively. This is a typical characteristic of recrystallized grains in low-SFE FCC metals and alloys, indicating that the microstructures of the HEA and MEA are fully recrystallized. It should be noted that owing to the limited step size (~30 nm) of the EBSD measurements, some annealing twins with very small thicknesses could not be captured; thus, the real values of the TB fraction could be higher. Despite these limitations, EBSD measurements can be beneficial for obtaining statistically reliable microstructural data, such as texture, from very large areas.

(4) Weak texture.

Fig. 9 **(c) and (g)** show the 1 1 1 pole figures for the CoCrFeMnNi HEA and CoCrNi MEA, respectively, after primary recrystallization. The texture intensities were as low as approximately 3.0 (i.e., weak texture), which is a typical characteristic of recrystallized low-SFE FCC metals and alloys. The symbols plotted in the figures are typical texture components, as summarized in Table 1. The higher-intensity parts in the pole figures coincided with some of the symbols, suggesting that the recrystallization texture of the HEA and MEA weakly maintained the torsion deformation texture. To further confirm the dominant texture component, the pole figures were converted to orientation distribution functions (ODFs) by harmonic series expansion and plotted as shown in Fig. 9 **(d) and (h)** for the CoCrFeMnNi HEA and CoCrNi MEA, respectively, together with the symbols in Table 1. In the HEA, the A* (A^*_1) texture, which is often observed in low-SFE FCC metals, was found to be the dominant component. This is in good agreement with a previous report on the same HEA processed using HPT at room temperature [13,32]. In the CoCrNi MEA, the C texture was found to be the dominant component of this material. Further studies are required to elucidate the textural differences between the HEA and MEA.

3.3. Grain boundary migration kinetics after primary recrystallization

After primary recrystallization, the HPT-processed materials were annealed at different temperatures and holding times to characterize the GB migration and grain growth behavior. The mean grain sizes (excluding TBs) of the HEA and MEA obtained at different temperatures and times are shown in Fig. 10 **(a) and (b)**, respectively. We employed the following grain growth kinetics model to calculate the apparent activation energies of grain growth in both the HEA and MEA [1]:

$$d^n - d_0^n = k_0 t \exp\left(-\frac{Q}{RT}\right) \tag{7}$$

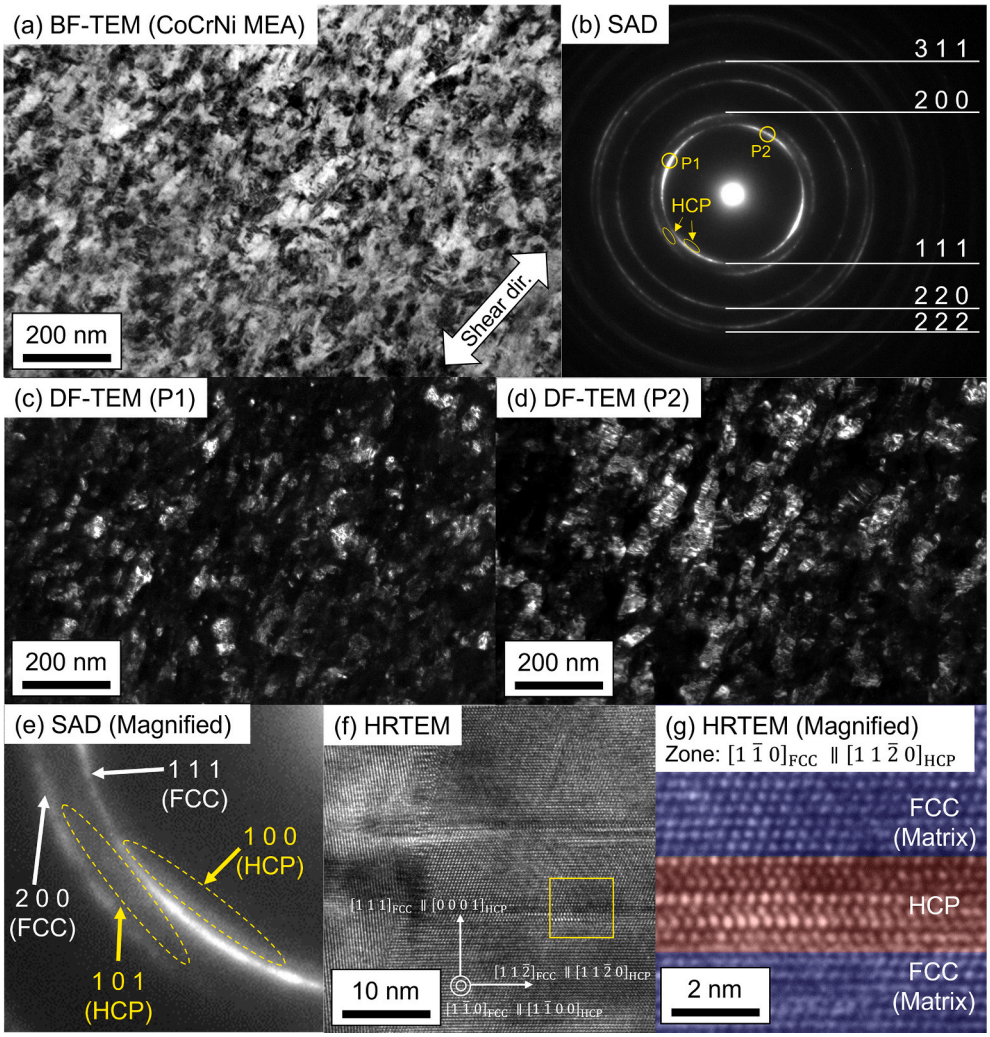

Fig. 3. (a) BF-TEM micrograph of the CoCrNi MEA processed by HPT. The shear direction is indicated by the double-headed arrow in the figure. (b) SAD pattern taken from the same area as shown in (a). The indices of each ring corresponding to an FCC structure are indicated in the figure. DF-TEM images formed by the diffraction spots of (c) P1 and (d) P2 in (b), acquired from the same area shown in (a). Fragmented grains with a high defect density and elongated along the shear direction are visible. (e) Magnified image of (b). The regions indicated by white and yellow arrows correspond to the reflections from FCC and HCP structures, respectively. (f) HRTEM micrograph of planar defects in the CoCrNi MEA processed by HPT. (g) Magnified image corresponding to the area indicated by the yellow rectangle in (f). Lattice structures corresponding to FCC and HCP (with eight atomic layers) structures are colored blue and red, respectively.

where d is the grain size after growth, d_0 is the grain size after primary recrystallization, n is the grain growth exponent, k_0 is a constant, t is the annealing time, Q is the apparent activation energy for grain growth, R is the gas constant, and T is the annealing temperature. Note that d and d_0 are the values without annealing twins because the mobility of twin boundaries is typically much lower than that of general HAGBs [1]. These data were fitted using **Equation (7)** to obtain the values of Q and n (summarized in Table 2). The n values for the HEA and MEA were found to be within the range of $2 < n < 3$, implying that both materials maintained an FCC single phase during annealing in the temperature range applied in the present work. As shown in Table 2, the activation energies of grain growth in the HEA (304 $kJmol^{-1}$) and MEA (308 $kJmol^{-1}$) were approximately three times higher than those of pure Ni (102 $kJmol^{-1}$) reported in the literature [39], suggesting sluggish GB migration kinetics in the HEAs and MEAs. Similar GB migration kinetics have been reported previously for other FCC HEAs and MEAs [14,15].

To better understand these experimental results, we performed atomistic hybrid MC/MD calculations to simulate the GB structures in the two-dimensional lattices of model HEAs. In the model, the atomic size difference (δ) of the constituent elements (i.e., lattice distortion), defined by **Equation (5)**, and the temperature are variable. We calculated the GB free volume (V_{GB} defined by **Equation (6)**), which exhibits a positive correlation with the GB mobility and GB energy [1], normalized by the magnitude of the Burgers vector (b) as a function of δ, as shown in Fig. 10 **(c)**. V_{GB} decreased with increasing δ. This is likely because atoms of different sizes can geometrically cancel out the lattice distortion in regions adjacent to GBs and consequently reduce V_{GB}. As severe lattice distortion is one of the special characteristics of HEAs and MEAs [6,7], the V_{GB} values of the present HEA and MEA are expected to be small. The data also indicate that decreases in temperature promoted the segregation of specific elements within a few atomic layers near the GBs (see the example in Fig. 10 **(d)**), with a simultaneous decrease in V_{GB}. This decrease in V_{GB} as a consequence of segregation was evidently due to specific elements having either large or small atomic sizes geometrically canceling V_{GB} and contributing to a further reduction in the total free energy of the system. It is also interesting to note that recent studies [40,41] have also pointed out that such smaller V_{GB} in HEAs/MEAs can increase the critical resolved shear stress for dislocation emissions from GBs, resulting in macroscopic yielding, which may cause greater grain refinement strengthening compared to conventional alloys with larger V_{GB}.

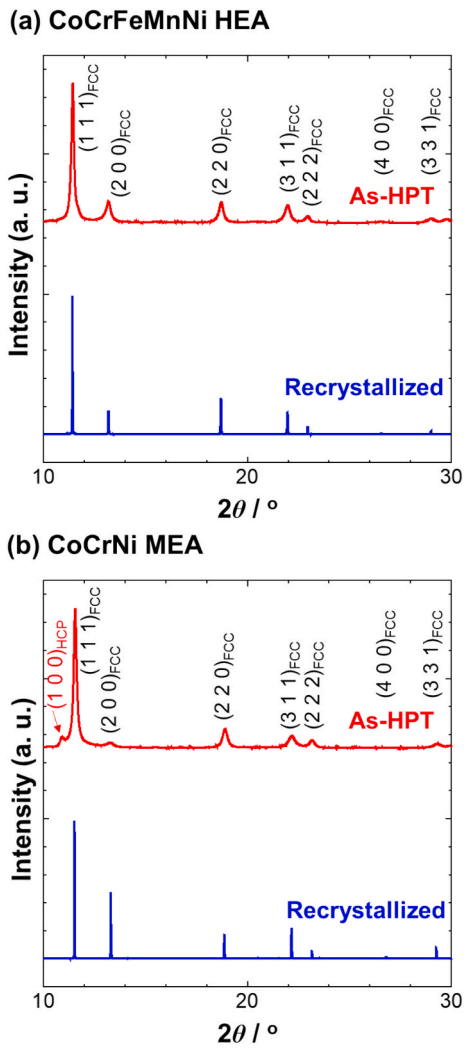

Fig. 4. XRD profiles of (a) the CoCrFeMnNi HEA and (b) CoCrNi MEA after HPT and after recrystallization at 800 °C for 10 s and 700 °C for 30 s, respectively. The peaks are indexed by corresponding lattice planes in FCC structures. The peak indicated by a red arrow in (b) corresponds to (100) reflection in an HCP structure.

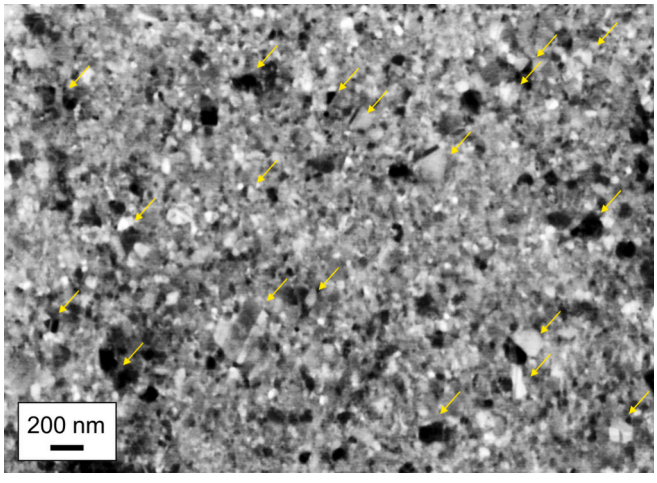

Fig. 5. SEM-BSE micrograph of the CoCrNi MEA processed by HPT and subsequently annealed at 700 °C for 10 s. The microstructure of this specimen was partially recrystallized, and nucleated recrystallized grains (indicated by yellow arrows) with annealing twins were found in some regions.

4. Discussion

4.1. Grain refinement during HPT process

As shown in Fig. 1, the microhardness of the HEA and MEA increased monotonically with increasing applied shear strain during the HPT. In this process, the grain size of the materials gradually decreased owing to grain subdivision [25,36,42]. Subsequently, the microhardness saturated, and the grain size of the materials remained unchanged with a further increase in shear strain. This phenomenon is generally observed in crystalline materials processed by various SPD processes and is attributed to the balance between the introduction and annihilation of lattice defects (dynamic recovery) during HPT. In pure metals, it is well established that the grain size after the saturation of microhardness is strongly correlated with factors controlling the dynamic recovery process, such as the deformation temperature relative to the melting point, diffusivity of vacancies, and SFE [43,44]. In particular, for FCC metals and alloys, it is widely believed that the contribution of the SFE to the grain size after microhardness saturation is significant. However, some studies [29,45] have pointed out that the correlation between the grain size after SPD processes and SFE in FCC alloys is weak. In fact, the grain sizes of the CoCrFeMnNi HEA and CoCrNi MEA with low SFEs (approximately 30 mJm^{-2} [33] and 20 mJm^{-2} [34], respectively) in the present study were much finer than those of Cu alloys and Ni alloys with similar SFEs values.

By contrast, Edalati *et al.* [29] reported that the grain size in HPT-processed FCC solid solution alloys is highly correlated with the extent (strength contribution) of solution strengthening rather than the SFE. As shown in Fig. 11 (reproduced based on data provided by Edalati *et al.* [29]), there is a clear correlation between the grain sizes of the HPT-processed FCC solid solution alloys (Al [46,47], Cu [48,49], Ni [50,51], and Pd [52] alloys) normalized by the Burgers vectors and the contribution of solution strengthening calculated using the Labusch model [53,54]. In a series of our previous studies, we demonstrated that solution strengthening in FCC HEAs/MEAs also follows Labusch-type models [7,55–59]. In Fig. 11, we also plotted the grain sizes of the HPT-processed CoCrFeMnNi HEA and CoCrNi MEA from the present study along with the solution strengthening extent (increase in the shear strength by solution strengthening normalized by the shear modulus, $\Delta\tau / G$) extracted from our previous report [7]. Interestingly, the data points for the HEA and MEA follow the same trend reported by Edalati *et al.* (solid black line). This suggests that dynamic recovery in FCC solid solutions, including HEAs/MEAs, is strongly affected by the presence of alloying elements. Because the concentration of alloying elements in HEAs/MEAs is significantly higher than that in conventional dilute alloys, it is expected that dynamic recovery in HEAs/MEAs is inhibited. As a result, extensive grain subdivision (fragmentation owing to the accumulation of defects) [36] occurs in HEAs/MEAs, leading to finer nanocrystalline microstructures compared to conventional dilute FCC alloys.

There are several possible explanations for the correlation between grain size after HPT and the presence of alloying elements in FCC solid solution alloys, including HEAs/MEAs. One is the chemical heterogeneity-induced variation in stacking fault width. Recent studies [60,61] have shown that the local width of stacking faults in FCC HEAs and MEAs can vary significantly because atoms of different elements occupy different lattice sites, causing local variations in the SFE on an atomistic scale. Dynamic recovery in these materials requires the cross-slip of screw dislocations through the shrinking of stacking faults into perfect dislocations, and parts with wider local stacking fault widths will inhibit the dynamic recovery in HEAs/MEAs. Another potential effect of alloying is stress-induced variation in the stacking fault width. Our recent studies [56,62,63] also suggested that the high flow stress (resulting from solution strengthening) of FCC HEAs/MEAs can exert different degrees of shear stress on leading/trailing partials, dynamically decreasing the apparent SFE, thereby inhibiting the cross-slip of dislocations. Furthermore, previous reports have shown that chemical

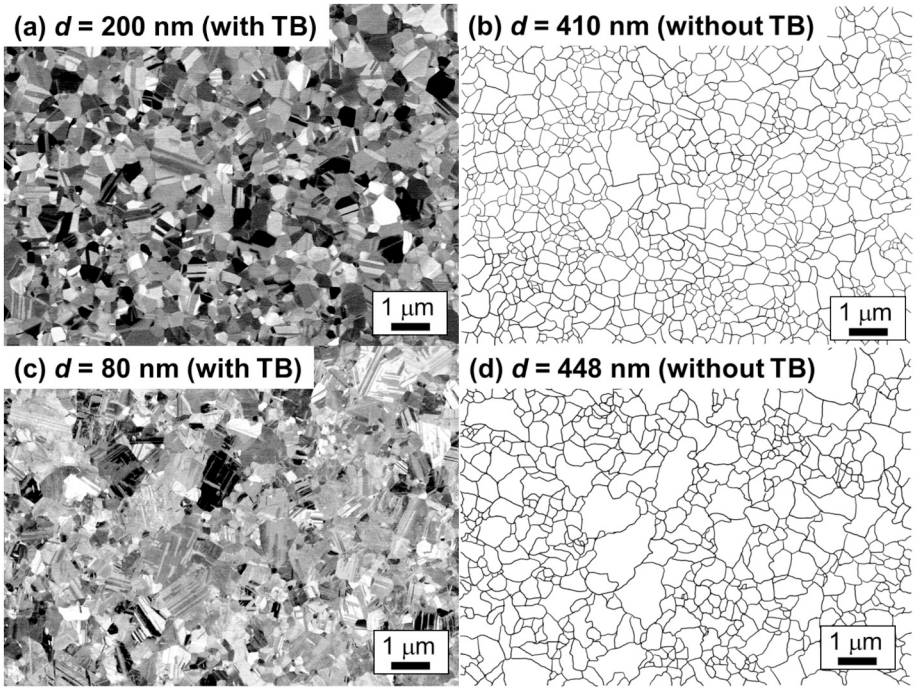

Fig. 6. SEM-BSE micrographs of (a) the CoCrFeMnNi HEA and (c) CoCrNi MEA after primary recrystallization. The mean grain sizes with annealing TBs are provided in the upper left of each image. Grain boundary maps for the (b) CoCrFeMnNi HEA and (d) CoCrNi MEA without TBs, corresponding to the same areas shown in (a) and (c), respectively. Mean grain sizes without TBs are provided in the upper left of each image.

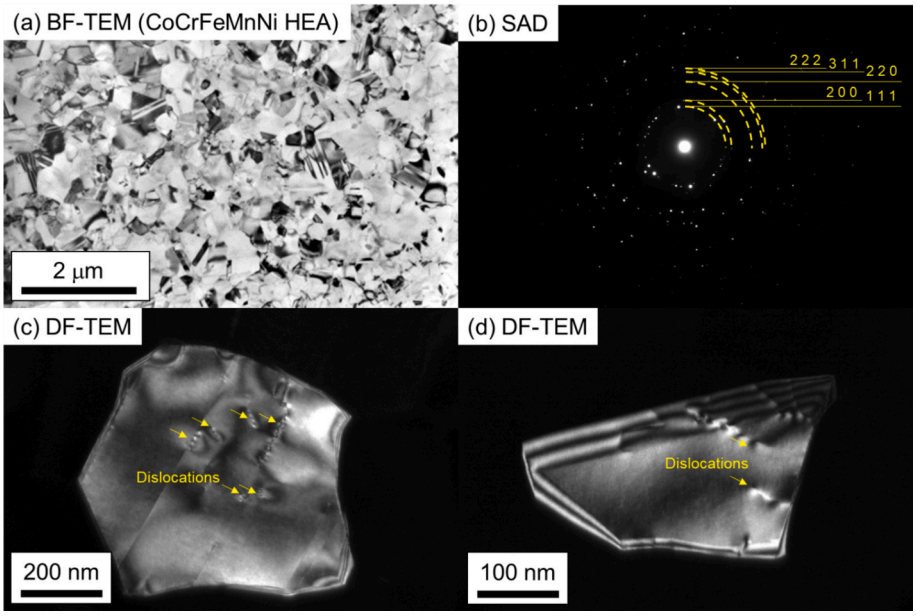

Fig. 7. (a) BF-TEM micrograph of the CoCrFeMnNi HEA processed by HPT and subsequently annealed at 800 °C for 10 s. Equiaxed grains with numerous annealing twins are visible. (b) SAD pattern obtained from the same area as shown in (a). Parts of the rings corresponding to the radial position of the 1 1 1, 2 0 0, 2 2 0, 3 1 1, and 2 2 2 reflections of an FCC structure are indicated in the figure by yellow dashed arcs. This pattern exhibits many spots, indicating that the material was fully recrystallized. (c, d) Typical DF-micrographs of recrystallized grains. It was confirmed that many of the grains contained a small number of dislocations.

interactions among alloying elements (known as solute–solute interaction or element-element interaction) can increase the activation energy required for the cross-slip of screw dislocations [64,65]. Although, to the best of our knowledge, there is no reliable experimental technique to directly capture such local interactions between stacking faults and alloying elements at this moment, our results indirectly prove that dynamic recovery is more suppressed in FCC HEAs/MEAs than in conventional dilute alloys and pure metals. Therefore, a higher dislocation density and finer grain size can be readily achieved in FCC HEAs/MEAs after SPD processes. This unique microstructure significantly affects the recrystallization behavior, as discussed in the subsequent sections.

4.2. Recrystallization mechanisms and critical nuclei size

In this section, we elucidate the rationale behind the achievement of significantly fine microstructures in the HEA and MEA after HPT and

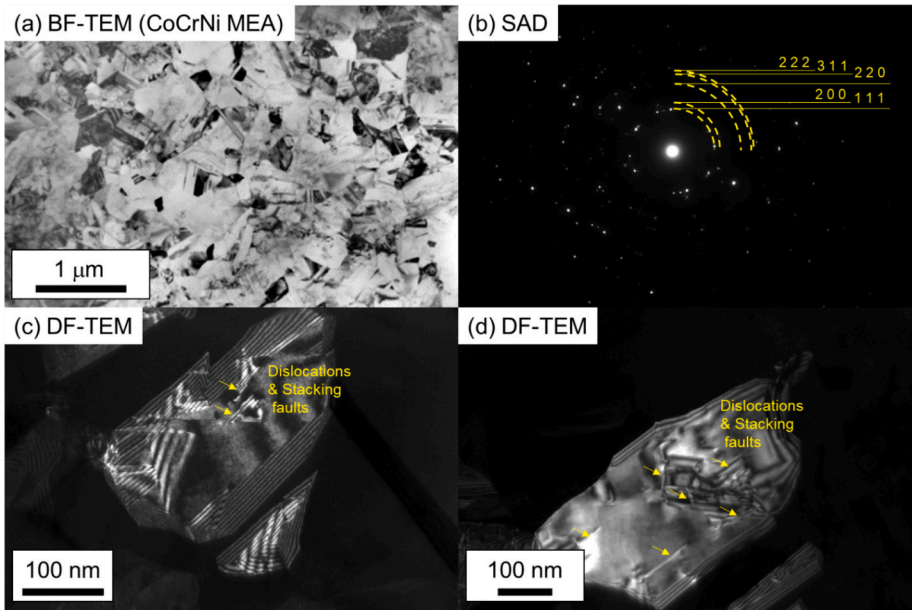

Fig. 8. (a) BF-TEM micrograph of the CoCrNi MEA processed by HPT and subsequently annealed at 700 °C for 30 s. Equiaxed grains with numerous annealing twins can be seen. (b) SAD pattern obtained from the same area as shown in (a). Parts of the rings corresponding to the radial position of the 1 1 1, 2 0 0, 2 2 0, 3 1 1, and 2 2 2 reflections of an FCC structure are indicated in the figure by yellow dashed arcs. This pattern exhibits many spots, indicating that the material was fully recrystallized. (c, d) Typical DF-micrographs of recrystallized grains, revealing that many of the grains contained a small number of dislocations and stacking faults.

annealing. In general, it is believed that potential nuclei of recrystallization exist in the deformed matrix [1]. Such nuclei should be domains that are surrounded by highly mobile HAGBs and have a lower dislocation density than the surrounding matrix, which develops under the process of grain subdivision during deformation and possibly subsequent recovery during annealing in some cases [66–68]. If there is a difference in dislocation density (i.e., stored elastic energy) between the interior and exterior of a nucleus, the migration of GBs (corresponding to coarsening of the nucleus) occurs towards the side with a higher dislocation density to reduce the total energy of the system, which is known as *strain-induced boundary migration* (SIBM) [1]. Through this continuous process, coarsening of the nuclei occurs, leading to recrystallization. The concept of potential nuclei present in a deformed matrix was first proposed by Cahn [66] and experimental evidence supporting this hypothesis has been reported. For instance, Yu *et al.* [67] investigated the recovery and recrystallization in heavily deformed pure aluminum with a particular focus on GB triple-junctions with Y-shapes formed from elongated grains in the deformed matrix. This study established that these triple junctions migrated during the early stage of annealing, accompanied by the annihilation of dislocations and the formation of equiaxed grains with a low dislocation density. Subsequently, coarsening of some of the equiaxed grains (i.e., recrystallization) was confirmed. Our recent work [68] using in situ TEM observations during heating confirmed the formation of nuclei from nanocrystalline microstructures in shear bands (resembling the microstructures in Figs. 2 and 3) in a cold-rolled CoCrFeMnNi HEA during the initial stage of annealing, followed by coarsening of the nuclei. This simple picture is also supported by our observation that the recrystallized grains in this study contained a small number of residual dislocations (Figs. 7 and 8), which were possibly introduced prior to recrystallization, and that the texture of the recrystallized microstructure was very similar to the deformation texture (Fig. 9).

Here, we consider a simple model in which there is a nucleus for recrystallization, defined as a domain with a low defect density (ρ') surrounded by HAGBs, in a deformed matrix with a high defect density (ρ), as illustrated in Fig. 12 **(a)**. For simplicity, a nucleus is modeled as a sphere with a radius of r, and the HAGBs are assumed to have a constant GB energy of γ_{GB}. Now, we consider that the nucleus grows, and the radius becomes (r + dr) from r. GB migration by SIBM (coarsening of nuclei) occurs based on the difference in the elastic energy stored by lattice defects between the interior (E') and exterior (E) of the nucleus as the thermodynamic driving force. In this case, the molar free energy change dG of the system can be expressed as

$$\mathrm{d}G(r) = \left(-\frac{4}{3}\pi(r+\mathrm{d}r)^3E + 4\pi(r+\mathrm{d}r)^2\gamma_{GB}\right) - \left(-\frac{4}{3}\pi r^3E' + 4\pi r^2\gamma_{GB}\right) \tag{8}$$

The first and second terms in brackets in **Equation (8)** represent the contributions of the bulk free energy and GB energy, respectively. Neglecting higher-order terms, **Equation (8)** can be simplified as

$$\frac{\mathrm{d}G(r)}{\mathrm{d}r}dr = \left(-4\pi r^2\Delta E + 8\pi r\gamma_{GB}\right)\mathrm{d}r \tag{9}$$

where $\Delta E = E - E'$. If dG is at a local maximum, $\left(\frac{\mathrm{d}G(r^*)}{\mathrm{d}r} = 0\right)$, the critical nucleus size ($d^* = 2r^*$) above which the nucleus can undergo stable growth is

$$d^* = \frac{4\gamma_{GB}}{\Delta E} \tag{10}$$

Assuming that the lattice defects that store elastic energy are mainly dislocations, ΔE can be expressed as

$$\Delta E = \alpha\mu b^2(\rho - \rho') \tag{11}$$

where α is a constant related to the line tension of dislocations, μ is the shear modulus, and b is the magnitude of the Burgers vector. If $\rho \gg \rho$' is assumed, **Equation (10)** can be rewritten as

$$d^* = \frac{4\gamma_{GB}}{\alpha\mu b^2\rho} \tag{12}$$

For FCC HEAs and MEAs, α was reported to be 0.06125 [69]. The μ values of CoCrFeMnNi HEA and CoCrNi MEA were reported as 80 GPa [70] and 91 GPa [71], respectively. The b values of the HEA and MEA were determined to be 0.2545 nm and 0.2520 nm, respectively, using

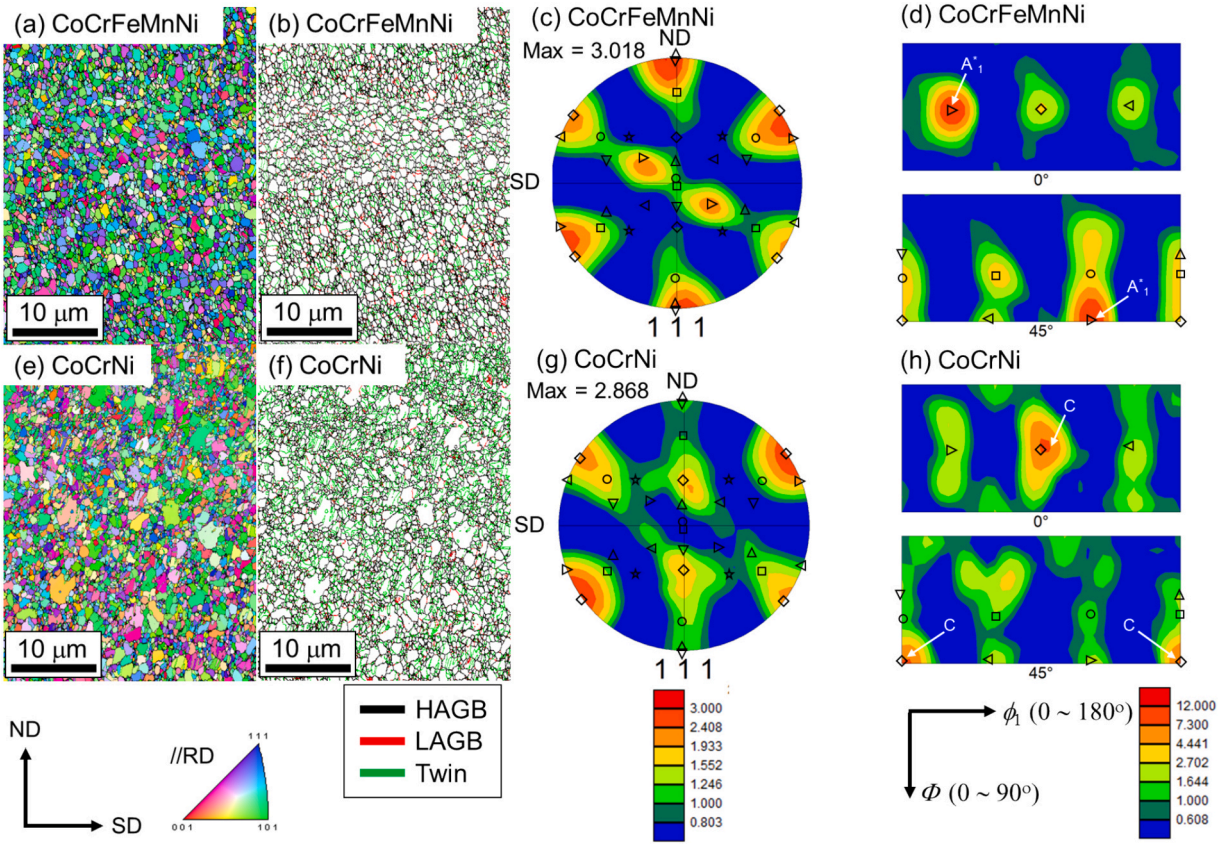

Fig. 9. EBSD inverse pole figure (IPF) maps for the (a) CoCrFeMnNi HEA and (b) CoCrNi MEA processed by HPT and subsequently annealed at 800 °C for 10 s and 700 °C for 30 s, respectively. SD, ND, and RD denote shear direction, radial direction and shear plane normal direction in HPT, respectively, in these figures. The colors in the IPF map indicate the orientation of grains along RD, and the color legend is also provided. Corresponding grain boundary (GB) maps for the (b) CoCrFeMnNi HEA and (f) CoCrNi MEA. The black, red, and green lines correspond to high-angle grain boundaries (HAGBs) (> 15°), low-angle grain boundaries (LAGBs), and twin boundaries (TBs), respectively. It should be noted that, due to the limited step size (~30 nm) of the EBSD measurements, some annealing twins with very small thickness could not be captured; thus, the real values of the twin boundary fraction can be higher. The 1 1 1 pole figures for the (c) CoCrFeMnNi HEA and (g) CoCrNi MEA based on (a) and (e), respectively. The symbols plotted together are typical texture components as summarized in Table 1. The orientation distribution function (ODF) maps for the (d) CoCrFeMnNi HEA and (h) CoCrNi MEA plotted based on (a) and (d), respectively. The maps were sectioned at φ2 = 0 and 45°. Bunge's definition of the Euler angle was used. The definition of the symbols plotted together is the same as in (b) and (e).

Table 1
Typical texture components in shear-deformed FCC metals extracted from literature [78]. SD and ND denote shear direction and shear plane normal direction, respectively.

Notation	Symbol	{*u v w*} ⊥ ND	<*h k l*> // SD
A_1	△	(1 1 –1)	[1 –1 0]
A_2	▽	(–1 –1 1)	[-1 1 0]
A^*_1	◁	(1 1 –1)	[2 –1 1]
A^*_2	▷	(1 –1 1)	[-2 –1 1]
B_1	○	(1 1 –2)	[1 –1 0]
B_2	□	(–1 –1 2)	[-1 1 0]
C	◇	(1 0 0)	[0 –1 1]
	☆	(1 0 0)	[0 0 1]

synchrotron XRD (Fig. 4). For instance, assuming $\gamma_{GB} = 1.0\ Jm^{-2}$ (a typical value for transition metals and their alloys) and a homogeneous distribution of dislocations in the as-HPT specimens, the critical size for the nuclei in the CoCrFeMnNi HEA was calculated to be 370 nm. We note that this value is much larger than the typical critical nucleus size for phase transformation (~ several nanometers). The formation of such large nuclei via thermal fluctuation of the atomic arrangement (such as in the case of phase transformation) is statistically unlikely. Therefore, it is reasonable to assume that potential nuclei are present in highly deformed regions with large misorientations such as shear bands, deformation bands, and vicinities of the original GBs. Such highly deformed regions can occur everywhere in SPD-processed materials. It should also be noted that nuclei larger than d^* would be expected to grow, whereas those smaller than d^* would not shrink (different from the case of nuclei for phase transformation). Instead, nuclei smaller than d^* were consumed by other growing nuclei (irreversible phenomena) to reduce the total free energy of the system.

In Fig. 12 **(b)**, we plot the critical nuclei size as a function of the dislocation density, ρ, over a range of possible GB energy values, γ_{GB}, for transition metals and HEAs [72], assuming a homogeneous distribution of dislocations in the as-HPT specimens. With increasing dislocation density, the critical nuclei size decreased, corresponding to a higher density of nuclei. The dislocation density in the HEA and MEA can be high because dynamic recovery is inhibited owing to the low SFE and characteristics of FCC HEAs/MEAs, as suggested in the previous section. The calculated values for the critical nuclei sizes of the materials are shown in the figure. These values were similar to the sizes of the nucleated grains, as shown in Fig. 5. We also indicate the mean grain sizes of the materials after HPT and after primary recrystallization. The grain sizes after HPT were smaller than the critical nuclei size, suggesting that the nuclei possibly developed through triple-junction migration accompanied by the annihilation of dislocations at the beginning of the annealing process, as confirmed by our in situ TEM observations of the recrystallization process [68]. The grain sizes of the recrystallized materials were larger than the critical size of the nuclei but were of the same order of magnitude. Hence, in the primary

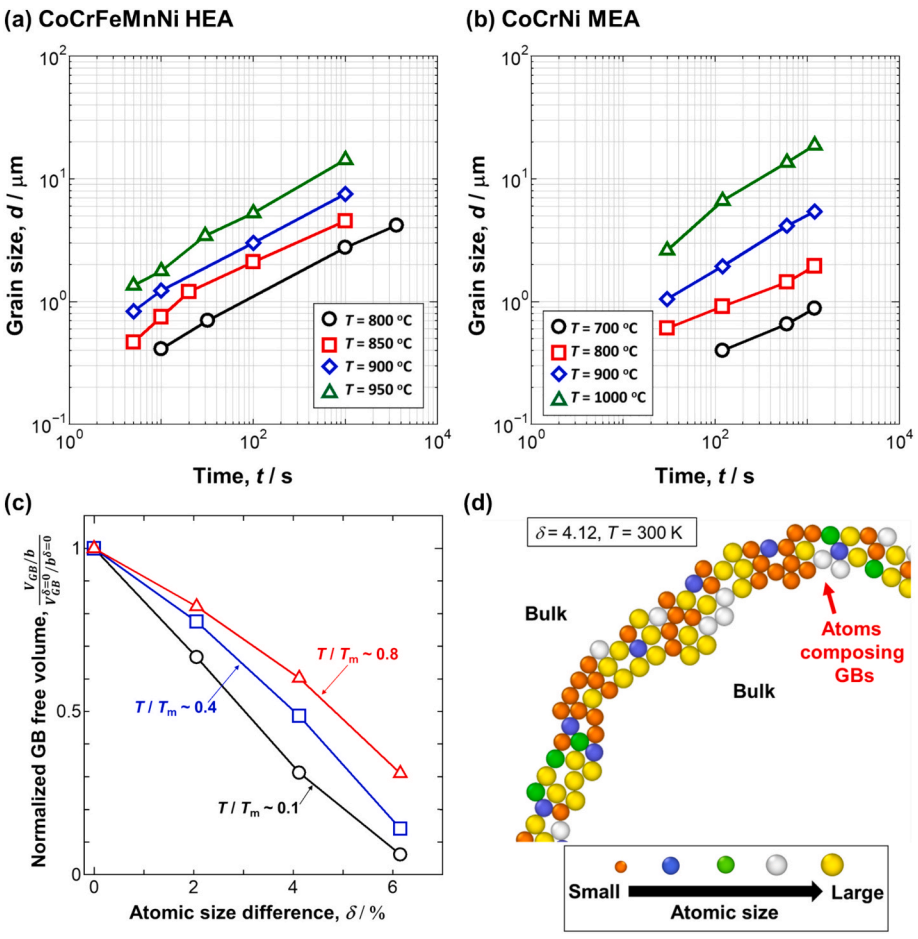

Fig. 10. Mean grain sizes of (a) the CoCrFeMnNi HEA and (b) CoCrNi MEA after primary recrystallization and after further annealing at different temperatures, plotted as functions of the holding time. (c) Normalized GB free volume of model HEAs as a function of the atomic size difference of the constituent elements (δ) at T/T_m values of approximately 0.1 (black circles), 0.4 (blue squares), and 0.8 (red triangles), as calculated by the hybrid MC/MD simulations. The V_{GB} values were first normalized by the magnitude of the Burgers vector to eliminate the effect of the system size and then normalized by the value for pure metal with $\delta = 0$. (d) A typical GB structure for a model HEA with $\delta = 4.12$ at 300 K as generated by the MC/MD simulations. This model comprises atoms of five different sizes.

Table 2
Activation energies of grain growth and growth exponents for pure Ni [39], the present CoCrNi MEA, and the present CoCrFeMnNi HEA calculated using Equation (7).

Materials	Activation energy, Q / kJmol^{-1}	Growth exponent, n
Pure Ni [39]	102	2.0
CoCrNi MEA	308	2.1
CoCrFeMnNi HEA	304	2.3

recrystallization process of the present HEA and MEA, only a slight growth of the nuclei occurred until they collided with one another because of the significantly high density of potential nuclei (smaller d^*). It should be noted that, in real microstructures, the distribution of dislocations cannot be perfectly homogeneous, and the density can be higher in highly deformed regions such as shear bands, deformation bands, and original grain boundaries. However, because of the ultrahigh applied strains of HPT and inhibited dynamic recovery in HEAs/MEAs, the distribution of dislocations can be more homogeneous than in conventional materials with conventional processes, as discussed later in Section 4.4. This is presumably why the simplified model calculation agreed well with our experimental observations.

4.3. Interaction between alloying elements and migrating grain boundaries

Our experimental results of grain growth kinetics and atomistic simulations clearly show that the grain boundary migration kinetics in HEAs/MEAs can be sluggish, possibly because of the geometrical cancellation of grain boundary free volumes, which reduces the mobility of boundaries. This massive solute drag, enhanced by severe lattice distortion, is considered to be a consequence of the interaction between alloying elements and migrating grain boundaries, which can be a unique characteristic of HEAs/MEAs.

If the velocities of GB migration and diffusion rate of alloying elements are comparable, segregation of alloying elements along the GBs is possible. According to the data shown in Fig. 10 **(a) and (b)**, the velocity of GB migration was estimated to be approximately 10^1 nm/s at the beginning of recrystallization. For instance, the mean grain size of CoCrFeMnNi HEA increased from 410 nm (excluding TBs) to approximately 700 nm in 20 s (Fig. 10(a)), giving an estimated velocity of 14.5 nm/s ($\sim 10^1$ nm/s). The velocity decreased in the later stage because of the decreased driving force for GB migration (i.e., GB surface energy). Based on the diffusion coefficients of each element in the HEA and MEA reported in the literature [73,74], the velocity of lattice diffusion was estimated to be 10^{-1} nm/s at similar temperatures, which is 10^2 times slower than that of GB migration. Hence, elemental segregation at GBs is unlikely to occur during recrystallization through lattice diffusion. However, the velocity of diffusion along GBs is approximately 10^1–10^2

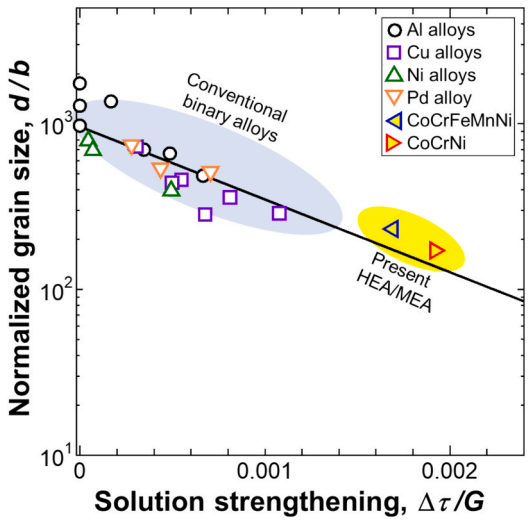

Fig. 11. Relationship between the extent of solution strengthening (increase in the shear strenght normalized by the shear modulus, calculated using the Labusch model) and the grain sizes of various HPT-processed FCC alloys normalized by the Burgers vector. The data points for conventional binary alloys (Al [46,47], Cu [48,49], Ni [50,51], and Pd [52] alloys) and the fitting line (black solid line) were extracted from the paper by Edalati et al [29]. The data points of the CoCrFeMnNi HEA and CoCrNi MEA in the present study are plotted together. The extent of solution strengthening for the HEA and MEA were extracted from our previous work [7].

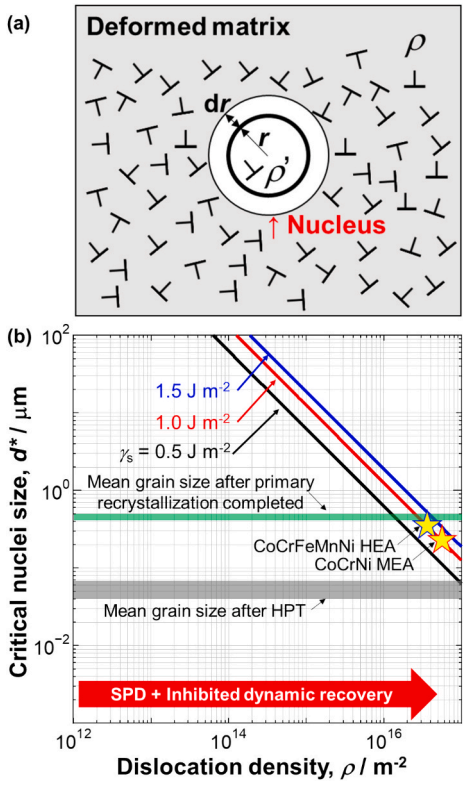

Fig. 12. (a) Schematic illustration of a potential nucleus in a deformed matrix. (b) Critical nuclei size as a function of dislocation density (ρ) for the possible value ranges of grain boundary energy (γ_s) in transition metals and HEAs [72]. The critical nuclei sizes (as calculated using Equation (12)) for the CoCrFeMnNi HEA and CoCrNi MEA are plotted together. The mean grain sizes of the HEA and MEA after HPT and after primary recrystallization are also indicated.

times higher than that of lattice diffusion [1,75]. Therefore, GB segregation of specific elements during recrystallization could possibly occur via diffusion along GBs. In fact, the GB segregation of certain elements (such as Co and Ni) has been reported to occur in the HEA [76] and MEA [77] at intermediate temperatures.

Although the present work does not provide direct evidence of elemental segregation at the GBs in the HEA and MEA annealed at high temperatures, these results at least clearly indicate that GBs can strongly interact with solute atoms of different sizes, even without such GB segregation. During GB migration, atoms jump across GBs, and if the solute atoms at the GBs have low potential energies (i.e., they interact strongly with the GBs), GB migration is inhibited. This phenomenon is known as *solute drag* [1]. In conventional dilute alloys, the solute drag effect is evident in low-angle (LA) GBs at low velocities [1]. However, our atomistic calculations suggest that in the case of high-alloy systems, this effect can be significant even in the case of HAGBs with high velocities because of the variety of alloying elements and the resulting severe lattice distortion. Therefore, sluggish GB migration can be considered a unique property of HEAs and MEAs, attributed to the massive solute drag enhanced by severe lattice distortion.

4.4. Microstructure evolution during deformation and recrystallization

Finally, to clarify the nature of the grain refinement in the present HEA and MEA during HPT and subsequent recrystallization annealing, here we consider the case of conventional heavy deformation processes, such as cold rolling, applied to conventional dilute alloys or pure metals (Fig. 13 **(a)**). In such processes, plastic deformation is microscopically heterogeneous, and many potential nuclei are mainly introduced at the original GBs, deformation bands, and shear bands, where the dislocation density and misorientations are locally large. The density of the potential nuclei in the deformed matrix is limited because dynamic recovery readily occurs during deformation. Consequently, nucleation proceeds both heterogeneously and sparsely, and the nuclei grow until they collide with one another, leading to a coarse-grained microstructure after primary recrystallization. Subsequently, grain growth occurs rapidly, resulting in further microstructural coarsening. The minimum mean grain size obtained by these processes is typically limited to several micrometers. In contrast, in the present study, we applied HPT to the HEA and MEA (Fig. 13 **(b)**). Compared with the above processes, we believe that there are several advantages for achieving finer microstructures, as follows: (1) In SPD processes such as HPT, domains with large misorientations are introduced throughout the material owing to the large strain. (2) Dynamic recovery during deformation is inhibited owing to the low SFE and to the characteristics of FCC HEAs/MEAs (as discussed in Section 4.1), leading to a very high dislocation density. Consequently, extensive grain subdivision occurs, and the density of the potential nuclei is expected to be much higher than that in the conventional case. Hence, nucleation occurs homogeneously and at a high density, resulting in the formation of FRex-UFG microstructures. (3) In addition, owing to the low SFE of the materials, annealing TBs with a high density further refine the microstructure. (4) Moreover, grain growth is suppressed owing to the sluggish GB migration enhanced by severe lattice distortion in the HEA and MEA (as discussed in Section 3.3). Therefore, fine microstructures can be easily maintained after primary recrystallization.

We note that (2–4) above can also be applied to the recrystallization behavior of FCC HEAs and MEAs processed by conventional deformation processes such as cold rolling. In such deformation processes, the nuclei of recrystallized grains are most likely to be distributed in the original GBs, deformation bands, and shear bands. Because of the inhibited dynamic recovery, the nucleation of recrystallized grains can occur at a higher density than in conventional FCC metals and alloys, leading to fine-grained microstructures. Therefore, Sun *et al.* [8] achieved FRex-UFG microstructures in a CoCrFeMnNi HEA only by cold rolling and annealing. Systematic investigation of recrystallization in cold-rolled FCC HEAs and MEAs in comparison with conventional alloys is our

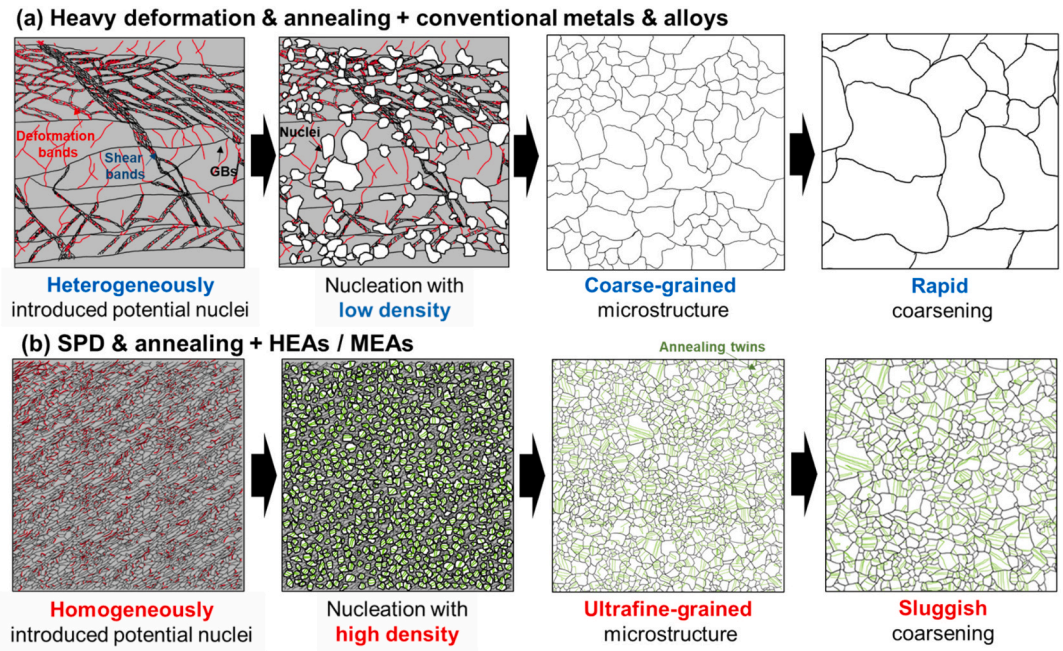

Fig. 13. Schematic illustration of microstructure evolution during annealing in the cases of (a) conventional heavy deformation processes applied to conventional metals and alloys and (b) severe plastic deformation process applied to HEAs and MEAs. The black and red lines indicate HAGBs and LAGBs, respectively, while the green lines indicate annealing TBs. The gray and white areas are deformed and recrystallized regions, respectively.

ongoing work and will be published elsewhere in the near future.

5. Conclusions

In the present study, we explored the unique characteristics of recrystallization in FCC HEAs/MEAs, along with the underlying mechanisms. Two representative materials, CoCrFeMnNi HEA and CoCrNi MEA, were processed using HPT at room temperature, followed by annealing at high temperatures. Their microstructures were systematically examined using electron microscopy. By combining experimental observations with atomistic simulations of grain boundaries in artificial HEAs, we clarified the following:

1. After HPT with five rotations at room temperature, the microhardness of the HEA and MEA was saturated. The HEA and MEA exhibited nanocrystalline microstructures with high dislocation densities, comprising elongated and fragmented grains with sizes of 58 nm and 43 nm, respectively, which are significantly finer than those observed in conventional FCC metals and dilute alloys. A strong correlation was identified between the grain size of the HPT-processed FCC alloys and the extent of solution strengthening. These findings suggest that extremely fine microstructures can be readily obtained in SPD-processed FCC HEAs/MEAs because of the inhibition of dynamic recovery, which is attributed to the high concentrations of alloying elements and low SFEs.
2. Upon annealing the HPT-processed HEA and MEA at high temperatures, FRex-UFG microstructures with FCC single-phase and high-density annealing twins were obtained after primary recrystallization. Notably, the mean grain sizes (without/with TBs) of the HEA and MEA were 410/200 nm and 448/80 nm, respectively, which are the smallest ever reported for fully recrystallized single-phase materials. The recrystallized grains contained a small number of residual dislocations and stacking faults, which were possibly introduced before nucleation, and the recrystallized specimens retained torsion deformation textures. Through comparison with a simple model, it was suggested that the density of nuclei for recrystallized grains in the HEA and MEA could be exceptionally high, resulting in minimal growth of the nuclei before they collide with one another and leading to the formation of FRex-UFG microstructures in the HEA and MEA.
3. The activation energies of grain growth in the HEA and MEA after primary recrystallization were 304 $kJmol^{-1}$ and 308 $kJmol^{-1}$, respectively, which were three times higher than that of pure Ni. This indicates sluggish GB migration kinetics in the HEAs/MEAs. Atomistic simulations revealed that the GB free volume decreased with an increase in the degree of lattice distortion in artificial HEAs. These results suggest that the GB mobility of the HEA and MEA can be low because of the massive solute drag effect of the GBs enhanced by severe lattice distortion, inducing geometrical cancellation of the GB free volumes.

In brief, we successfully achieved significantly fine grain sizes (with TBs) in the HEA and MEA (80 nm for CoCrNi MEA and 200 nm for CoCrFeMnNi HEA), which are the smallest among the FRex single-phase FCC materials reported to date. The distinctive characteristics of FCC HEAs and MEAs, such as inhibited dynamic recovery and sluggish GB migration, which are closely linked to the high concentrations of alloying elements that alter the local chemical environment around lattice defects, were found to exert a significant influence on their grain refinement behavior during deformation and recrystallization. These effects are associated with an increased density of recrystallization nuclei and the suppression of microstructural coarsening. These findings are related to the interaction between the alloying elements and lattice defects in the microstructural evolution during deformation and annealing. Thus, we believe that the knowledge in the present study can be universally applicable to various alloys and will help us to construct a more generalized theory of recrystallization and related phenomena. The exceptional ultra-grain-refinement behavior found in HEAs and MEAs will therefore broaden the possibility of microstructural control of metallic materials, allowing us to approach the ultimate limit of grain refinement through SPD and recrystallization.

CRediT authorship contribution statement

Shuhei Yoshida: Writing – original draft, Validation, Investigation,

Funding acquisition, Formal analysis, Data curation, Conceptualization. **Nokeun Park:** Writing – review & editing, Investigation, Funding acquisition, Formal analysis, Data curation, Conceptualization. **Kohei Shiotani:** Writing – review & editing, Visualization, Validation, Investigation, Formal analysis, Data curation. **Yu Bai:** Writing – review & editing, Supervision. **Tomoaki Niiyama:** Writing – review & editing, Supervision. **Akinobu Shibata:** Writing – review & editing, Supervision. **Tomotsugu Shimokawa:** Writing – review & editing, Supervision, Software, Methodology, Funding acquisition. **Nobuhiro Tsuji:** Writing – review & editing, Supervision, Resources, Project administration, Funding acquisition, Conceptualization.

Declaration of competing interest

The authors declare that they have no known competing financial interests or personal relationships that could have appeared to influence the work reported in this paper.

Acknowledgments

This work was financially supported by the Elements Strategy Initiative for Structural Materials (ESISM, No. JPMXP0112101000) (NT), Japan Society for the Promotion of Science (JSPS) the Fund for the Promotion of Joint International Research (International Leading Research) (No. JP23K20037 (SY, NT)), the Grant-in-Aid for Scientific Research on Innovative Area "High Entropy Alloys" (No. JP18H05453 (TS), JP18H05455 (NT)), Scientific Research (S) (No. JP15H05767 (NT)), Scientific Research (B) (No. JP25K00050 (SY)), Early-Career Scientists (No. JP22K14501 (SY)), Research Activity Start-up (No. JP21K20487 (SY)), and JSPS Research Fellow (No. JP18J20766 (SY)), all through the Ministry of Education, Culture, Sports, Science and Technology (MEXT), Japan. This study was also supported by the Nano & Material Technology Development Program through the National Research Foundation of Korea (NRF) grant funded by the Korean government (Ministry of Science and ICT) (No. RS-2024-00451579 (NP)). The financial supports are gratefully appreciated.

Synchrotron X-ray diffraction experiments were performed at the BL46XU of SPring-8 with the approval of the Japan Synchrotron Radiation Research Institute (JASRI) (Proposal No. 2019B1801). The authors acknowledge Dr. Masugu Sato (JASRI) and Prof. Hiroki Adachi (University of Hyogo) for their technical assistance with the synchrotron radiation experiments. The authors note that this work is a part (Chapter 4) of the doctoral dissertation of SY.

Appendix A. Supplementary data

Supplementary data to this article can be found online at https://doi.org/10.1016/j.matdes.2025.114622.

Data availability

Data will be made available on request.

References

[1] A.D. Rollett, G.S. Rohrer, F.J. Humphreys. Recrystallization and related annealing phenomena, 3rd Edition, Elsevier, 2017.
[2] E.P. George, D. Raabe, R.O. Ritchie, High-entropy alloys, Nat. Rev. Mater. 4 (2019) 515–534, https://doi.org/10.1038/s41578-019-0121-4.
[3] E.P. George, W.A. Curtin, C.C. Tasan, High entropy alloys: a focused review of mechanical properties and deformation mechanisms, Acta Mater. 188 (2019) 435–474, https://doi.org/10.1016/j.actamat.2019.12.015.
[4] H. Inui, K. Kishida, Z. Chen, Recent Progress in our Understanding of phase Stability, Atomic Structures and Mechanical and Functional Properties of High-Entropy Alloys, Mater Trans 63 (2022) 394–401, https://doi.org/10.2320/MATERTRANS.MT-M2021234.
[5] B. Cantor, Multicomponent high-entropy Cantor alloys, Prog Mater Sci (2020) 100754. https://doi.org/10.1016/j.pmatsci.2020.100754.
[6] S. Yoshida, T. Bhattacharjee, Y. Bai, N. Tsuji, Friction stress and Hall-Petch relationship in CoCrNi equi-atomic medium entropy alloy processed by severe plastic deformation and subsequent annealing, Scr. Mater. 134 (2017) 33–36, https://doi.org/10.1016/j.scriptamat.2017.02.042.
[7] S. Yoshida, T. Ikeuchi, T. Bhattacharjee, Y. Bai, A. Shibata, N. Tsuji, Effect of elemental combination on friction stress and Hall-Petch relationship in face-centered cubic high / medium entropy alloys, Acta Mater. 171 (2019) 201–215, https://doi.org/10.1016/j.actamat.2019.04.017.
[8] S.J. Sun, Y.Z. Tian, H.R. Lin, X.G. Dong, Y.H. Wang, Z.J. Zhang, Z.F. Zhang, Enhanced strength and ductility of bulk CoCrFeMnNi high entropy alloy having fully recrystallized ultrafine-grained structure, Mater. Des. 133 (2017) 122–127, https://doi.org/10.1016/j.matdes.2017.07.054.
[9] P.P. Bhattacharjee, G.D. Sathiaraj, M. Zaid, J.R. Gatti, C. Lee, C.W. Tsai, J.W. Yeh, Microstructure and texture evolution during annealing of equiatomic CoCrFeMnNi high-entropy alloy, J. Alloys Compd. 587 (2014) 544–552, https://doi.org/10.1016/j.jallcom.2013.10.237.
[10] G.D. Sathiaraj, P.P. Bhattacharjee, Analysis of microstructure and microtexture during grain growth in low stacking fault energy equiatomic CoCrFeMnNi high entropy and Ni-60 wt.%Co alloys, J Alloys Compd 637 (2015) 267–276, https://doi.org/10.1016/j.jallcom.2015.02.184.
[11] G.D. Sathiaraj, P.P. Bhattacharjee, Materials Characterization effect of cold-rolling strain on the evolution of annealing texture of equiatomic CoCrFeMnNi high entropy alloy, Mater Charact 109 (2015) 189–197, https://doi.org/10.1016/j.matchar.2015.09.027.
[12] G.D. Sathiaraj, M.Z. Ahmed, P.P. Bhattacharjee, Microstructure and texture of heavily cold-rolled and annealed fcc equiatomic medium to high entropy alloys, J. Alloys Compd. 664 (2016) 109–119, https://doi.org/10.1016/j.jallcom.2015.12.172.
[13] G.D. Sathiaraj, A. Pukenas, W. Skrotzki, Texture formation in face-centered cubic high-entropy alloys, J. Alloys Compd. 826 (2020) 154183, https://doi.org/10.1016/j.jallcom.2020.154183.
[14] W.H. Liu, Y. Wu, J.Y. He, T.G. Nieh, Z.P. Lu, Grain growth and the Hall–Petch relationship in a high-entropy FeCrNiCoMn alloy, Scr. Mater. 68 (2013) 526–529, https://doi.org/10.1016/j.scriptamat.2012.12.002.
[15] Y.-C. Huang, C.-H. Su, S.-K. Wu, C. Lin, A Study on the Hall–Petch Relationship and grain Growth Kinetics in FCC-Structured High/Medium Entropy Alloys, Entropy 21 (2019) 297, https://doi.org/10.3390/e21030297.
[16] S. Praveen, J. Basu, S. Kashyap, R.S. Kottada, Exceptional resistance to grain growth in nanocrystalline CoCrFeNi high entropy alloy at high homologous temperatures, J. Alloys Compd. 662 (2016) 361–367, https://doi.org/10.1016/j.jallcom.2015.12.020.
[17] M.H. Mohammad-Ebrahimi, A. Zarei-Hanzaki, H.R. Abedi, S.M. Vakili, C. K. Soundararajan, Decelerated grain growth kinetic and effectiveness of Hall-Petch relationship in a cold-rolled non-equiatomic high entropy alloy, J. Alloys Compd. (2021) 159849, https://doi.org/10.1016/j.jallcom.2021.159849.
[18] B.D.S. Rathod, R. Gholizadeh, M.H. Park, S. Yoshida, N. Tsuji, Effect of Zr micro-alloying on microstructure refinement and mechanical property of CoCrNi medium-entropy alloy processed by high-pressure torsion and subsequent annealing, J. Mater. Sci. 59 (2024) 5736–5753, https://doi.org/10.1007/S10853-023-09244-2/FIGURES/11.
[19] S. Yoshida, G. Yamashita, T. Ikeuchi, Y. Bai, A. Shibata, N. Tsuji, Grain size dependent deformation microstructure evolution and work-hardening in CoCrNi medium entropy alloy, Journal of Alloys and Metallurgical Systems 8 (2024) 100123, https://doi.org/10.1016/J.JALMES.2024.100123.
[20] Q. He, S. Yoshida, N. Tsuji, Characteristic strengthening mechanisms in body-centered cubic refractory high/medium entropy alloys, Scr. Mater. 231 (2023) 115442, https://doi.org/10.1016/J.SCRIPTAMAT.2023.115442.
[21] A. Azushima, R. Kopp, A. Korhonen, D.Y. Yang, F. Micari, G.D. Lahoti, P. Groche, J. Yanagimoto, N. Tsuji, A. Rosochowski, A. Yanagida, Severe plastic deformation (SPD) processes for metals, CIRP Ann. Manuf. Technol. 57 (2008) 716–735, https://doi.org/10.1016/j.cirp.2008.09.005.
[22] Y. Zhu, K. Ameyama, P.M. Anderson, I.J. Beyerlein, H. Gao, H.S. Kim, E. Lavernia, S. Mathaudhu, H. Mughrabi, R.O. Ritchie, N. Tsuji, X. Zhang, X. Wu, Heterostructured materials: superior properties from hetero-zone interaction, Mater Res Lett 9 (2021) 1–31, https://doi.org/10.1080/21663831.2020.1796836.
[23] R.Z. Valiev, N.A. Krasilnikov, N.K. Tsenev, Plastic deformation of alloys with submicron-grained structure, Mater. Sci. Eng. A 137 (1991) 35–40, https://doi.org/10.1016/0921-5093(91)90316-F.
[24] F. Otto, A. Dlouhý, K.G. Pradeep, M. Kuběnová, D. Raabe, G. Eggeler, E.P. George, Decomposition of the single-phase high-entropy alloy CrMnFeCoNi after prolonged anneals at intermediate temperatures, Acta Mater. 112 (2016) 40–52, https://doi.org/10.1016/j.actamat.2016.04.005.
[25] T. Yamashita, R. Gholizadeh, S. Yoshida, N. Tsuji, Effect of Deformation and subsequent Heat Treatment on Sigma-phase Precipitation and Mechanical Property of CoCrFeMnNi High Entropy Alloy, Mater. Trans. 65 (2024) 1015–1024, https://doi.org/10.2320/MATERTRANS.MT-MA2024005.
[26] G. Ribárik, Modeling of diffraction patterns based on microstructural properties, Eötvös University Budapest, 2008.
[27] A. Heczel, M. Kawasaki, J.L. Lábár, J. il Jang, T.G. Langdon, J. Gubicza, Defect structure and hardness in nanocrystalline CoCrFeMnNi High-Entropy Alloy processed by High-Pressure Torsion, J Alloys Compd 711 (2017) 143–154. https://doi.org/10.1016/j.jallcom.2017.03.352.
[28] O. Renk, R. Pippan, Saturation of Grain Refinement during Severe Plastic Deformation of Single phase Materials: Reconsiderations, Current Status and Open Questions, Mater Trans 60 (2019) 1270–1282, https://doi.org/10.2320/matertrans.MF201918.

[29] K. Edalati, D. Akama, A. Nishio, S. Lee, Y. Yonenaga, J.M. Cubero-Sesin, Z. Horita, Influence of dislocation–solute atom interactions and stacking fault energy on grain size of single-phase alloys after severe plastic deformation using high-pressure torsion, Acta Mater. 69 (2014) 68–77, https://doi.org/10.1016/j.actamat.2014.01.036.

[30] J. Miao, C.E. Slone, T.M. Smith, C. Niu, H. Bei, M. Ghazisaeidi, G.M. Pharr, M. J. Mills, The evolution of the deformation substructure in a Ni-Co-Cr equiatomic solid solution alloy, Acta Mater. 132 (2017) 35–48, https://doi.org/10.1016/j.actamat.2017.04.033.

[31] C.E. Slone, S. Chakraborty, J. Miao, E.P. George, M.J. Mills, S.R. Niezgoda, Influence of deformation induced nanoscale twinning and FCC-HCP transformation on hardening and texture development in medium-entropy CrCoNi alloy, Acta Mater. 158 (2018) 38–52, https://doi.org/10.1016/j.actamat.2018.07.028.

[32] W. Skrotzki, A. Pukenas, E. Odor, B. Joni, T. Ungar, B. Völker, A. Hohenwarter, R. Pippan, E.P. George, Microstructure, texture, and strength development during high-pressure torsion of crmnfeconi high-entropy alloy, Crystals (basel) 10 (2020), https://doi.org/10.3390/cryst10040336.

[33] N.L. Okamoto, S. Fujimoto, Y. Kambara, M. Kawamura, Z.M.T. Chen, H. Matsunoshita, K. Tanaka, H. Inui, E.P. George, Size effect, critical resolved shear stress, stacking fault energy, and solid solution strengthening in the CrMnFeCoNi high-entropy alloy, Sci. Rep. 6 (2016) 35863, https://doi.org/10.1038/srep35863.

[34] G. Laplanche, A. Kostka, C. Reinhart, J. Hunfeld, G. Eggeler, E.P. George, Reasons for the superior mechanical properties of medium-entropy CrCoNi compared to high-entropy CrMnFeCoNi, Acta Mater. 128 (2017) 292–303, https://doi.org/10.1016/j.actamat.2017.02.036.

[35] J. Koike, D.M. Parkin, Koike J., Parkin D.M., N. M., Crystall-to-amorphous transformation of NiTi induced by cold rolling, J Mater Res 5 (1990) 1414–1418.

[36] D.A. Hughes, N. Hansen, High angle boundaries formed by grain subdivision mechanisms, Acta Mater. 45 (1997) 3871–3886, https://doi.org/10.1016/S1359-6454(97)00027-X.

[37] R. Saha, R. Ueji, N. Tsuji, Fully recrystallized nanostructure fabricated without severe plastic deformation in high-Mn austenitic steel, Scr. Mater. 68 (2013) 813–816, https://doi.org/10.1016/j.scriptamat.2013.01.038.

[38] Y. Tian, A. Shibata, Z. Zhang, N. Tsuji, Ductility Sensitivity to Stacking Fault Energy and grain size in Cu–Al Alloys, Mater Res Lett 3831 (2016) 1–6, https://doi.org/10.1080/21663831.2015.1136969.

[39] M.C. Iordache, S.H. Whang, Z. Jiao, Z.M. Wang, Grain growth kinetics in nanostructured nickel, Nanostruct. Mater. 11 (1999) 1343–1349, https://doi.org/10.1016/S0965-9773(00)00427-X.

[40] K. Shiotani, T. Niiyama, T. Shimokawa, Dislocation Emission from Grain Boundaries in High-Entropy Alloys: Influence of Atomic Composition at Grain Boundaries, Mater. Trans. 61 (2020) 1272–1279, https://doi.org/10.2320/MATERTRANS.Z-M2020819.

[41] K. Shiotani, T. Niiyama, T. Shimokawa, Atomistic study on dislocation emission from segregated grain boundaries in high-entropy alloys, Phys. Rev. Mater. 7 (2023) 123606, https://doi.org/10.1103/PHYSREVMATERIALS.7.123606/FIGURES/13/MEDIUM.

[42] R. Gholizadeh, S. Yoshida, Y. Bai, S. Kurokawa, A. Shibata, N. Tsuji, Global understanding of deformation behavior in CoCrFeMnNi high entropy alloy under high-strain torsion deformation at a wide range of elevated temperatures, Acta Mater. 243 (2023) 118514, https://doi.org/10.1016/J.ACTAMAT.2022.118514.

[43] F.A. Mohamed, A dislocation model for the minimum grain size obtainable by milling, Acta Mater. 51 (2003) 4107–4119, https://doi.org/10.1016/S1359-6454(03)00230-1.

[44] F.A. Mohamed, S.S. Dheda, On the minimum grain size obtainable by high-pressure torsion, Mater. Sci. Eng. A 558 (2012) 59–63, https://doi.org/10.1016/J.MSEA.2012.07.066.

[45] K. Edalati, Z. Horita, High-pressure torsion of pure metals: Influence of atomic bond parameters and stacking fault energy on grain size and correlation with hardness, Acta Mater. 59 (2011) 6831–6836, https://doi.org/10.1016/J.ACTAMAT.2011.07.046.

[46] S. Lee, Z. Horita, Enhancement of strength and ductility of Al-Ag alloys processed by high-pressure torsion and aging, Metall. Mater. Trans. A Phys. Metall. Mater. Sci. 44 (2013) 3221–3231, https://doi.org/10.1007/S11661-013-1664-4/METRICS.

[47] A. Bachmaier, M. Hafok, R. Pippan, Rate Independent and Rate Dependent Structural Evolution during Severe Plastic Deformation, Mater. Trans. 51 (2010) 8–13, https://doi.org/10.2320/MATERTRANS.MB200912.

[48] Y.H. Zhao, Y.T. Zhu, X.Z. Liao, Z. Horita, T.G. Langdon, Tailoring stacking fault energy for high ductility and high strength in ultrafine grained Cu and its alloy, Appl. Phys. Lett. 89 (2006), https://doi.org/10.1063/1.2356310/120730.

[49] X.H. An, Q.Y. Lin, S.D. Wu, Z.F. Zhang, R.B. Figueiredo, N. Gao, T.G. Langdon, The influence of stacking fault energy on the mechanical properties of nanostructured Cu and Cu–Al alloys processed by high-pressure torsion, Scr. Mater. 64 (2011) 954–957, https://doi.org/10.1016/J.SCRIPTAMAT.2011.01.041.

[50] S. Lee, Z. Horita, Annealing Behavior of FeNi Alloy Processed by High-pressure Torsion, Mater. Sci. Forum 667–669 (2011) 313–318, https://doi.org/10.4028/WWW.SCIENTIFIC.NET/MSF.667-669.313.

[51] P.L. Sun, Y.H. Zhao, J.C. Cooley, M.E. Kassner, Z. Horita, T.G. Langdon, E. J. Lavernia, Y.T. Zhu, Effect of stacking fault energy on strength and ductility of nanostructured alloys: an evaluation with minimum solution hardening, Mater. Sci. Eng. A 525 (2009) 83–86, https://doi.org/10.1016/J.MSEA.2009.06.030.

[52] L. Kurmanaeva, Y. Ivanisenko, J. Markmann, C. Kübel, A. Chuvilin, S. Doyle, R. Z. Valiev, H.J. Fecht, Grain refinement and mechanical properties in ultrafine grained Pd and Pd–Ag alloys produced by HPT, Mater. Sci. Eng. A 527 (2010) 1776–1783, https://doi.org/10.1016/J.MSEA.2009.11.001.

[53] R. Labusch, A statistical theory of solid solution hardening, Phys. Status Solidi 41 (1970) 659–669.

[54] R. Labusch, Statistische theorien der mischkristallhärtung, Acta Metall. 20 (1972) 917–927, https://doi.org/10.1016/0001-6160(72)90085-5.

[55] A. Lavakumar, S. Yoshida, J. Punyafu, S. Ihara, Y. Chong, H. Saito, N. Tsuji, M. Murayama, Yield and flow properties of ultra-fine, fine, and coarse grain microstructures of FeCoNi equiatomic alloy at ambient and cryogenic temperatures, Scr. Mater. 230 (2023) 115392, https://doi.org/10.1016/J.SCRIPTAMAT.2023.115392.

[56] S. Yoshida, T. Ikeuchi, Y. Bai, A. Shibata, N. Hansen, X. Huang, N. Tsuji, Deformation microstructures and strength of face-centered cubic high/medium entropy alloys, IOP Conf. Ser.: Mater. Sci. Eng. 580 (2019) 012053.

[57] M.P.M.P. Agustianingrum, S. Yoshida, N. Tsuji, N. Park, Effect of aluminum addition on solid solution strengthening in CoCrNi medium-entropy alloy, J. Alloys Compd. 781 (2019) 866–872, https://doi.org/10.1016/j.jallcom.2018.12.065.

[58] B. Yin, S. Yoshida, N. Tsuji, W.A. Curtin, Yield strength and misfit volumes of NiCoCr and implications for short-range-order, Nat. Commun. 11 (2020) 2507, https://doi.org/10.1038/s41467-020-16083-1.

[59] K. Inoue, S. Yoshida, N. Tsuji, Direct observation of local chemical ordering in a few nanometer range in CoCrNi medium-entropy alloy by atom probe tomography and its impact on mechanical properties, Phys. Rev. Mater. 5 (2021) 085007, https://doi.org/10.1103/PHYSREVMATERIALS.5.085007/FIGURES/5/MEDIUM.

[60] T.M. Smith, M.S. Hooshmand, B.D. Esser, F. Otto, D.W. McComb, E.P. George, M. Ghazisaeidi, M.J. Mills, Atomic-Scale Characterization and Modeling of 60° Dislocations in a High Entropy Alloy, Acta Mater. 110 (2016) 352–363, https://doi.org/10.1016/j.actamat.2016.03.045.

[61] S.I. Rao, C. Woodward, T.A. Parthasarathy, O. Senkov, Atomistic simulations of dislocation behavior in a model FCC multicomponent concentrated solid solution alloy, Acta Mater. 134 (2017) 188–194, https://doi.org/10.1016/j.actamat.2017.05.071.

[62] S. Yoshida, R. Fu, W. Gong, T. Ikeuchi, Y. Bai, Z. Feng, G. Wu, A. Shibata, N. Hansen, X. Huang, N. Tsuji, Grain orientation dependence of deformation microstructure evolution and mechanical properties in face-centered cubic high/medium entropy alloys, IOP Conf. Ser.: Mater. Sci. Eng. 1249 (2022) 012027, https://doi.org/10.1088/1757-899X/1249/1/012027.

[63] S. Yoshida, R. Fu, W. Gong, T. Ikeuchi, Y. Bai, Z. Feng, G. Wu, A. Shibata, N. Hansen, X. Huang, N. Tsuji, Characteristic deformation microstructure evolution and deformation mechanisms in face-centered cubic high/medium entropy alloys, Acta Mater. 283 (2025) 120498, https://doi.org/10.1016/J.ACTAMAT.2024.120498.

[64] W.G. Nöhring, W.A. Curtin, Dislocation cross-slip in fcc solid solution alloys, Acta Mater. 128 (2017) 135–148, https://doi.org/10.1016/j.actamat.2017.02.027.

[65] W.G. Nöhring, W.A. Curtin, Cross-slip of long dislocations in FCC solid solutions, Acta Mater. 158 (2018) 95–117, https://doi.org/10.1016/j.actamat.2018.05.027.

[66] R.W. Cahn, A new theory of recrystallization nuclei, Proc. Phys. Soc. London, Sect. A 63 (1950) 323–336, https://doi.org/10.1088/0370-1298/63/4/302.

[67] T. Yu, N. Hansen, X. Huang, Linking recovery and recrystallization through triple junction motion in aluminum cold rolled to a large strain, Acta Mater. 61 (2013) 6577–6586, https://doi.org/10.1016/j.actamat.2013.07.040.

[68] B. Guo, R.K. Ray, S. Yoshida, Y. Bai, N. Tsuji, In-situ observations of static recrystallization and texture formation in a cold-rolled CoCrFeMnNi high entropy alloy, Scr. Mater. 215 (2022) 114706, https://doi.org/10.1016/J.SCRIPTAMAT.2022.114706.

[69] C. Varvenne, A. Luque, W.A. Curtin, Theory of strengthening in fcc high entropy alloys, Acta Mater. 118 (2016) 164–176, https://doi.org/10.1016/j.actamat.2016.07.040.

[70] K. Tanaka, T. Teramoto, R. Ito, Monocrystalline elastic constants of fcc-CrMnFeCoNi high entropy alloy, MRS Adv., Materials Research Society (2017) 1429–1434, https://doi.org/10.1557/adv.2017.76.

[71] K. Jin, Y.F. Gao, H. Bei, Intrinsic properties and strengthening mechanism of monocrystalline Ni-containing ternary concentrated solid solutions, Mater. Sci. Eng. A 695 (2017) 74–79, https://doi.org/10.1016/j.msea.2017.04.003.

[72] M. Vaidya, K.G. Pradeep, B.S. Murty, G. Wilde, S.V. Divinski, Radioactive isotopes reveal a non sluggish kinetics of grain boundary diffusion in high entropy alloys, Sci. Rep. 7 (2017) 1–11, https://doi.org/10.1038/s41598-017-12551-9.

[73] K.Y. Tsai, M.H. Tsai, J.W. Yeh, Sluggish diffusion in Co-Cr-Fe-Mn-Ni high-entropy alloys, Acta Mater. 61 (2013) 4887–4897, https://doi.org/10.1016/j.actamat.2013.04.058.

[74] K. Jin, C. Zhang, F. Zhang, H. Bei, Influence of compositional complexity on interdiffusion in Ni-containing concentrated solid-solution alloys, Mater Res Lett 6 (2018) 293–299, https://doi.org/10.1080/21663831.2018.1446466.

[75] H. Mehrer, Diffusion in Solids, Springer, Berlin, Heidelberg (2007), https://doi.org/10.1007/978-3-540-71488-0.

[76] K. Ming, L. Li, Z. Li, X. Bi, J. Wang, Grain boundary decohesion by nanoclustering Ni and Cr separately in CrMnFeCoNi high-entropy alloys, Sci Adv 5 (2019) eaay0639, https://doi.org/10.1126/sciadv.aay0639.

[77] Y.J. Li, A. Kostka, A. Savan, A. Ludwig, Phase decomposition in a nanocrystalline CrCoNi alloy, Scr. Mater. 188 (2020) 259–263, https://doi.org/10.1016/j.scriptamat.2020.07.054.

[78] F. Montheillet, M. Cohen, J.J. Jonas, Axial stresses and texture development during the torsion testing of Al, Cu and α-Fe, Acta Metall. 32 (1984) 2077–2089, https://doi.org/10.1016/0001-6160(84)90187-1.